condensed matter

MDPI

Article

Ground States of Heisenberg Spin Clusters from a Cluster-Based Projected Hartree–Fock Approach

Shadan Ghassemi Tabrizi [1,2,*] and Carlos A. Jiménez-Hoyos [1,*]

[1] Department of Chemistry, Wesleyan University, Middletown, CT 06459, USA
[2] Department of Chemistry, University of Potsdam, D-14476 Potsdam, Germany
* Correspondence: shadan.ghassemi@uni-potsdam.de (S.G.T.); cjimenezhoyo@wesleyan.edu (C.A.J.-H.)

Abstract: Recent work on approximating ground states of Heisenberg spin clusters by projected Hartree–Fock theory (PHF) is extended to a cluster-based ansatz (cPHF). Whereas PHF variationally optimizes a site–spin product state for the restoration of spin- and point-group symmetry, cPHF groups sites into discrete clusters and uses a cluster-product state as the broken-symmetry reference. Intracluster correlation is thus already included at the mean-field level, and intercluster correlation is introduced through symmetry projection. Variants of cPHF differing in the broken and restored symmetries are evaluated for ground states and singlet-triplet gaps of antiferromagnetic spin rings for various cluster sizes, where cPHF in general affords a significant improvement over ordinary PHF, although the division into clusters lowers the cyclical symmetry. In contrast, certain two- or three-dimensional spin arrangements permit cluster groupings compatible with the full spatial symmetry. We accordingly demonstrate that cPHF yields approximate ground states with correct spin- and point-group quantum numbers for honeycomb lattice fragments and symmetric polyhedra.

Keywords: molecular magnetism; spin hamiltonians; quantum-chemical methods; symmetry-projection

Citation: Ghassemi Tabrizi, S.; Jiménez-Hoyos, C.A. Ground States of Heisenberg Spin Clusters from a Cluster-Based Projected Hartree–Fock Approach. *Condens. Matter* **2023**, *8*, 18. https://doi.org/10.3390/condmat8010018

Academic Editor: Krzysztof Wohlfeld

Received: 6 January 2023
Accepted: 26 January 2023
Published: 3 February 2023

1. Introduction

The calculation of magnetic properties of exchange-coupled spin clusters, e.g., molecules with multiple open-shell transition-metal centers bridged by diamagnetic ligands [1,2], from the Heisenberg model, $\hat{H} = \sum_{i<j} J_{ij} \hat{\mathbf{s}}_i \cdot \hat{\mathbf{s}}_j$, usually relies on approximations, because exact diagonalization (ED) is only feasible for small systems. The ground state and perhaps a few excited states are needed to interpret electron-paramagnetic resonance (EPR) or inelastic neutron scattering (INS) spectra or to assess other low-temperature properties [3]. The density matrix renormalization group (DMRG [4]) is the most important variational method for ground states of one-dimensional (1D) systems (rings or chains) but is less suitable for 2D coupling topologies. The scarcity of computationally affordable and easily applicable alternatives motivated our recent exploration of projected Hartree–Fock theory (PHF [5]) for ground states of Heisenberg spin clusters [6]. PHF can be used in a black-box manner and has a mean-field (HF) scaling, with a prefactor depending on the size of the symmetry-projection grid. In finite spin systems, PHF restores spin (S) and point-group (PG) symmetry from a general product state. For a collection of $s = \frac{1}{2}$ sites, this broken-symmetry reference state is simply a three-dimensional spin configuration [6]. PHF yields rather accurate ground-state wave functions for symmetric rings with a moderate number of sites N and large local spin s and predicts reasonably accurate singlet-triplet gaps. Limitations become evident for larger rings, where the accuracy decreases [6]. PHF indeed recovers zero correlation energy per site in the thermodynamic limit $N \to \infty$. In other words, the method is not size extensive [7]. To ameliorate this problem and enable a more accurate treatment of larger systems by variational symmetry-projection methods, one could either adopt a multicomponent ansatz, where the broken-symmetry reference is a linear combination of nonorthogonal mean-field states [8], or work with a cluster basis

that grants more flexibility than ordinary PHF, while still optimizing just a single reference. We pursue the latter option, which we call cPHF. Note, however, that both strategies could be combined into a multicomponent cPHF ansatz, which may be pursued in future work. For other correlated spin-cluster approaches (coupled-cluster and many-body perturbation theory) and for further literature on related methods, see, e.g., [9]. Note that the cluster mean-field is the same mean-field used in cluster extensions of dynamical mean-field theory [10] (DMFT). In this work, however, rather than attempting to obtain the interacting Green's function, we use a variational ansatz to develop correlations in the ground state wave function using symmetry breaking and restoration. While symmetry breaking and restoration are somewhat limited in the flexibility they incorporate into the ansatz, it may be enough to obtain high-quality ground state wavefunctions for small systems with high symmetry, such as the ones considered in this work.

2. Theory and Computations

PHF optimizes a broken-symmetry mean-field state $|\Phi\rangle$ for the application of a symmetry projector $\hat{P}$ [5]. In cPHF, $|\Phi\rangle$ is a product of individual cluster states $|\Phi_i\rangle$:

$$|\Phi\rangle = \prod_{i=1}^{Q} |\Phi_i\rangle, \tag{1}$$

where Q is the total number of clusters. As an example, for a cluster comprising two $s = \frac{1}{2}$ sites, the structure of $|\Phi_i\rangle$ is given in Equation (2).

$$|\Phi_i\rangle = c_{i,1}|\downarrow\downarrow\rangle + c_{i,2}|\downarrow\uparrow\rangle + c_{i,3}|\uparrow\downarrow\rangle + c_{i,4}|\uparrow\uparrow\rangle \tag{2}$$

The $|\Phi_i\rangle$ is independently optimized to minimize the variational energy, Equation (3), of the projected state $|\Psi\rangle = \hat{P}|\Phi\rangle$:

$$E = \frac{\langle\Psi|\hat{H}|\Psi\rangle}{\langle\Psi|\Psi\rangle} = \frac{\langle\Phi|\hat{H}\hat{P}|\Phi\rangle}{\langle\Phi|\hat{P}|\Phi\rangle} \,. \tag{3}$$

The site-permutation invariance [11] of spin Hamiltonians representing systems with spatial symmetry (rings, symmetric polyhedra, etc.) is here referred to as point-group (PG) symmetry. Each level is thus characterized by its total spin S and its PG-label Γ. To recover a substantial fraction of the correlation energy for all but the smallest systems, it is mandatory to combine S- with PG-projection in PHF [6,12]. In the PG-projector $\hat{P}_\Gamma$ of Equation (3) (we consider only one-dimensional irreducible representations Γ), h is the order of the group, $\chi_\Gamma(g)$ is the character of group element g, and $\hat{R}_g$ is the respective symmetry operation [13].

$$\hat{P}_\Gamma = \frac{1}{h}\sum_{g=1}^{h} \chi_\Gamma^*(g)\hat{R}_g \tag{4}$$

Multidimensional irreducible representations become relevant for projection onto $S > 0$ sectors. The projector $\hat{P}_m^S$ for spin S and magnetic quantum number m (the $\hat{S}_z$ eigenvalue) is expanded in terms of transfer operators $\hat{P}_{mk}^S$,

$$\left|\Psi_m^S\right\rangle = \hat{P}_m^S|\Phi\rangle = \sum_k f_k \hat{P}_{mk}^S|\Phi\rangle \,, \tag{5}$$

which are conveniently parameterized by Euler angles [14],

$$\hat{P}_{mk}^S = \frac{2S+1}{8\pi^2}\iiint d\alpha d\beta d\gamma \sin(\beta) D_{mk}^{S*}(\alpha,\beta,\gamma) e^{-i\alpha\hat{S}_z} e^{-i\beta\hat{S}_y} e^{-i\gamma\hat{S}_z} \,. \tag{6}$$

For a given $|\Phi\rangle$, the coefficients f_k (Equation (5)) correspond to the lowest-energy solution of the generalized eigenvalue problem for the Hamiltonian $\hat{H}$ in the nonorthogonal ba-

sis spanned by $\{\hat{P}^S_{mk}|\Phi\rangle\}$, $k = -S, -S+1, ..., +S$ [12]. For combined S- and PG-projection, the projector is a product, $\hat{P} = \hat{P}^S_m \hat{P}_\Gamma$ (spin rotations commute with site permutations). In the trivial case where the projector is the identity, $\hat{P} = \hat{1}$, that is, if no symmetry projection is performed, cPHF is equivalent to cHF, also called cluster mean-field theory [9,15]. If each cluster comprises just one site, cPHF becomes equivalent to PHF, specifically, the "single fermion" variety of PHF presented in [6]. Finally, note that cPHF trivially yields the exact ground state in the chosen symmetry sector (S, Γ) if all sites are contained in a single cluster or if there are no couplings between clusters.

In quantum-chemical terminology, $|\Phi\rangle$ is of generalized HF type (GHF [16]) if it completely breaks spin symmetry. An unrestricted HF (UHF) state also breaks total spin symmetry (that is, $|\Phi\rangle$ is not an eigenfunction of $\hat{\mathbf{S}}^2$) but conserves $\hat{S}_z$. In a UHF-type reference, each cluster has a defined z-projection m_i. Different clusters may have different m_i, which add up to the total $\hat{S}_z$ eigenvalue, $m = \sum_i m_i$. Compared to complete spin-symmetry breaking in GHF, the number of variational parameters is reduced in UHF. As an example, a general $m_i = 0$ state of an $s = \frac{1}{2}$ dimer is a superposition of only two basis states, as shown in Equation (7):

$$|\Phi_i\rangle = c_{i,1}|{\downarrow\uparrow}\rangle + c_{i,2}|{\uparrow\downarrow}\rangle \,. \tag{7}$$

PHF variants that restore S- or PG-symmetry from a GHF- or UHF-type reference are called SGHF, PGSUHF, etc. In cPHF, the cluster size q may be appended, e.g., SGHF(2) denotes a cluster-based SGHF calculation with dimers. For a given grouping, the lowest variational energy is obtained when working with the largest symmetry group (PGSGHF). We do not include complex-conjugation symmetry [5,17] in the cPHF scheme, because this involves a more complicated formalism [6,18,19] and has comparatively small effects for Heisenberg systems [6].

Self-consistent field (SCF, [5,6,19,20]) and gradient-based optimization ([12,21] and references cited therein) are two different strategies for the optimization of $|\Phi\rangle$. In the SCF approach, the local cluster states $|\Phi_i\rangle$ result from successively building and diagonalizing an effective Fock matrix for each cluster. We found that reaching SCF convergence is often challenging in cPHF and therefore prefer gradient-based optimization, where each $|\Phi_i\rangle$ is parameterized in terms of a Thouless rotation from an initial guess $|\Phi^0_i\rangle$. Details are provided in Appendix A. With q sites of spin s, the number of real variational parameters that define a general Thouless rotation for a single cluster is $N_{\mathrm{var}} = 2[(2s+1)^q - 1]$, leading to a total of $N_{\mathrm{var}} = 2Q \cdot [(2s+1)^q - 1]$ for Q clusters (not counting the f_k coefficients for $S > 0$, cf. Equation (5)). Note, however, that the Thouless parameterization, though convenient, is slightly redundant [6] with respect to S-projection from a GHF-type reference $|\Phi\rangle$, because global spin rotations as well as certain gauge transformations of $|\Phi\rangle$ leave the spin-projected state unchanged [22].

The local cluster basis of dimension $(2s+1)^q$ would have to be truncated for large clusters, e.g., by considering a limited number of lowest levels of the intracluster Hamiltonian. As an example, such a scheme could make a treatment of the Mn_{70} or Mn_{84} single-molecule magnets (with $N = 70$ or $N = 84$ $s = 2$ sites) feasible in terms of a $q = 7$ division [23] but is beyond the scope of this work.

As recommended previously [20], we discretized transfer operators, Equation (6), with a combined Lebedev-Laikov [24] and Trapezoid integration grid. For S-projection from a UHF-type reference, the evaluation of integrals over Euler angles α and γ is trivial [25], and integration over β employs a Gauss–Legendre grid. A computational parallelization of the summation over the grid is trivial [20]. The quality of S-projection can be checked by computing $\langle\Psi|\hat{\mathbf{S}}^2|\Psi\rangle$ from a sum of spin-pair correlation functions (SPCFs), as shown in Equation (8):

$$\left\langle \hat{\mathbf{S}}^2 \right\rangle = Ns(s+1) + 2\sum_{i<j} \langle \hat{\mathbf{s}}_i \cdot \hat{\mathbf{s}}_j \rangle \,. \tag{8}$$

We ensured that $\left\langle \hat{\mathbf{S}}^2 \right\rangle$ deviates by $< 10^{-6}$ from the ideal value of $S(S+1)$. Details on the calculation of SPCFs are provided in Appendix B.

Figure 1 illustrates that cluster formations are in general not fully compatible with spatial symmetry, meaning that working with the cyclic C_N group (or the dihedral group D_N that additionally includes vertical C_2 axes) of spin rings with N sites would involve complicated transformations between different cluster bases; on a similar note, complicated transformations between different coupling schemes prevent the combined use of the full spin- and point-group symmetry in ED [26]. A division in terms of q neighbors thus reduces the cyclical symmetry of rings according to $C_N \to C_{N/q}$ or $D_N \to D_{N/q}$. For example, for $q = 2$, sectors k and $(k + \frac{N}{2})\mathrm{mod}N$ of group C_N (the crystal momentum k indicates the eigenvalue $\exp(-i2\pi k/N)$ of the cyclic permutation $\hat{C}_N$) belong to the same sector of group $C_{N/2}$. Thus, a $k = 0$ state in $C_{N/2}$ is generally a mixture of $k = 0$ (Mulliken label $\Gamma = \mathrm{A}$) and $k = \frac{N}{2}$ ($\Gamma = \mathrm{B}$) in C_N. This, however, does not imply that cPHF wave functions will significantly break symmetry with respect to the full point group (see Results section).

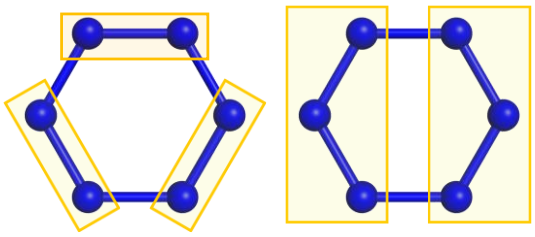

Figure 1. Two cluster groupings in an $N = 6$ ring. Dihedral symmetry is broken by dimerization $(D_6 \to D_3)$ or trimerization $(D_6 \to D_2)$. The respective reduced symmetry groups can be employed in cPHF.

From the perspective of molecular magnetism, symmetry reduction through cluster formation may not be a major concern, because the cyclic-symmetry order of existing ring-like molecules is often lower than the number of open-shell ions. For example, the mere six-fold rotational symmetry of an Fe_{18} ring (studied by INS in [27]) suggests a treatment in terms of six equivalent clusters, each hosting three neighboring $s = \frac{5}{2}$ sites, which represent three chemically inequivalent Fe^{III} ions. Furthermore, Mn_{70} and Mn_{84} tori, the largest single-molecule magnets known to date, have repeat units of 14 Mn^{III} ions (s = 2), but the pattern of isotropic couplings in the Heisenberg model suggests a partitioning into two inequivalent types of clusters with seven sites each [23].

In contrast, it is straightforward to use all spatial symmetries in cPHF that keep clusters intact, meaning that a given operation transforms all sites of one cluster into sites of a specific second cluster. Operations associated with internal site permutations do not pose a problem. For example, vertical $\hat{C}_2$ rotations in the dihedral group of rings involve such internal permutations; see Appendix A for details. The Results section additionally presents selected systems (honeycomb lattice fragments and symmetric polyhedra) permitting cluster groupings that are fully symmetry-compatible if operations associated with internal permutations are considered.

Unless noted otherwise, all clusters (total number $Q = N/q$) are equivalent by symmetry and contain the same number of sites q with a uniform local spin s, although these are not requirements for the application of cPHF. It is usually reasonable to construct clusters from neighboring (interacting) sites to recover a substantial amount of correlation energy already at the mean-field level. In the absence of intracluster interactions, cHF recovers the ordinary HF (classical spin, $q = 1$) solution. With respect to variational symmetry projection in cPHF, the cluster ansatz offers more flexibility than $q = 1$ (ordinary PHF), even when there are no intracluster interactions (see Results section).

The relative correlation energy, $0 \leq p \leq 1$, defined in Equation (9),

$$p = \frac{E_{\mathrm{cPHF}} - E_{\mathrm{HF}}}{E_0 - E_{\mathrm{HF}}} \,, \tag{9}$$

is an accuracy measure of cPHF for ground states, where E_0 is the exact result (ED), and E_{HF} refers to the classical solution, e.g., $E_{\mathrm{HF}} = -NJs^2$ for the Néel configuration in a ring. All benchmark systems treated here have a nondegenerate $S = 0$ ground state. Energies are reported in units of the uniform nearest-neighbor coupling constant $J = 1$ (antiferromagnetic coupling).

In cases where the system size prohibits a comparison with exact energies, we compare cPHF against a cluster-variant of second-order perturbation theory (cPT2). The (nonvariational) cPT2 corrected energy is given by Equation (10),

$$E_{\mathrm{cPT2}} = E_{\mathrm{cHF}} + \frac{\sum_{ab} \left| \langle \Phi_{\mathrm{cHF}} | \hat{H} | \Phi_{ab} \rangle \right|^2}{E_{\mathrm{cHF}} - E_{ab}} \,, \tag{10}$$

where $E_{\mathrm{cHF}} = \langle \Phi_{\mathrm{cHF}} | \hat{H} | \Phi_{\mathrm{cHF}} \rangle$, $E_{ab} = \langle \Phi_{ab} | \hat{H} | \Phi_{ab} \rangle$, and $|\Phi_{ab}\rangle$ is obtained from $|\Phi_{\mathrm{cHF}}\rangle$ through excitations a and b in two neighboring (directly interacting) clusters. In other words, $|\Phi_{ab}\rangle$ is a doubly excited cluster mean-field state. The denominator in the second term of Equation (10) is of Epstein–Nesbet type [28]. For cluster size $q = 1$ and $s = \frac{1}{2}$, such PT2 corrections were considered for the truncated icosahedron in [29]. Alternatively, one could apply Rayleigh–Schrödinger perturbation theory in a cluster basis, using differences of Fock-like orbital energies in the denominator, as seen in [9] (for the $s = \frac{1}{2}$ square lattice) and [30] (for the single-band Hubbard model).

3. Results and Discussion

For antiferromagnetic $s = \frac{1}{2}$ spin rings, honeycomb lattice fragments, and four tetrahedral or icosahedral polyhedra, we compare ground-state energies and SPCFs from different variants of cPHF against exact results (where available). In addition, we briefly consider singlet-triplet gaps in spin rings and larger local spin (up to $s = 2$) in polyhedra and explore how the quality of predictions depends on the cluster size or shape. Rather than deriving specific new insights on any of these systems, our aim is to investigate the potential of cPHF as a variational black-box method with a cluster mean-field scaling.

3.1. Symmetric Rings

As in our previous work [6], we choose rings with $N = 6, 12, 18, 24, 30$ sites as benchmark systems to compare against ED but restrict attention to the least classical case $s = \frac{1}{2}$, which had proven to be most problematic for ordinary PHF ($q = 1$) [6].

We note in passing that, in contrast to dimers formed from neighboring sites (see Theory section), clusters composed of diametrically opposite sites are indeed compatible with the full D_N symmetry. Figure 2 illustrates that the cyclic $\hat{C}_N$ operation leaves all clusters intact and exchanges sites in one dimer. For $N = 12$, C_NSGHF(2) with such a partitioning yields the exact $S = 0$ ground state (exact within numerical double precision) in each k sector ($k = 0, 1, \ldots, N - 1$), whereas C_NSGHF(1) turned out to be exact in sectors $k = 1, 3, 5, 7, 9, 11$ only [6]. This shows that the cluster ansatz is somewhat more flexible with respect to variational symmetry projection, even though HF(2) is equivalent to HF(1) due to the lack of intracluster interactions. For larger rings, the described pairing of the most distant sites does not provide a sizable improvement over PHF(1) and shall not be discussed further.

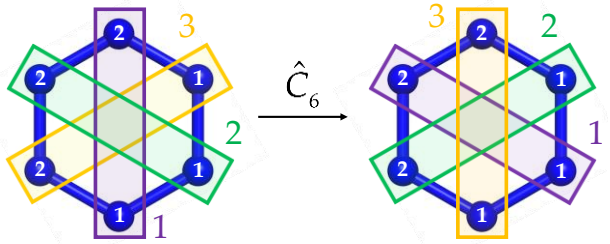

Figure 2. Dimers of diametrically opposite sites conserve the symmetry of rings (group D_6 in this example). A cyclic permutation interchanges sites in the last cluster (cluster 3, yellow box).

We construct clusters comprising $q = 2, 3, 6$ neighbors (Figure 3), corresponding to the common divisors of N, thus reducing the point group accessible to cPHF, that is, $D_N \to D_Q$, where $Q = N/q$. Rings with even N lack frustration and adopt UHF-type solutions in cHF. In contrast, for odd N (not studied here), frustration gives rise to genuine GHF solutions breaking $\hat{S}_z$ symmetry.

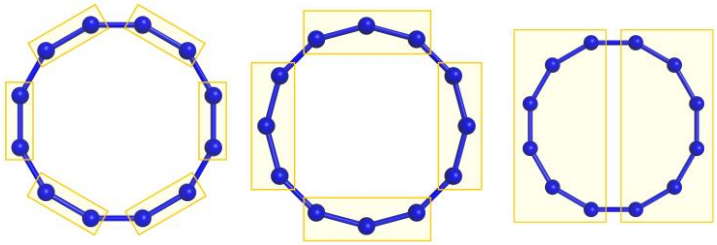

Figure 3. Clusters of size $q = 2, 3, 6$ in an $N = 12$ ring.

It is simple to show that HF(2) produces a product of singlets, $s_i = 0$. We observed that local singlets are also formed in HF(6). Consequently, E_{HF} is a sum of the ground-state energies of the individual clusters: $E_{\mathrm{HF}(2)} = -\frac{3}{4}Q$, and $E_{\mathrm{HF}(6)} = -2.4936Q$ (for $Q > 1$). In contrast, for $q = 3$, all clusters assume z-projections $|m_i| = \frac{1}{2}$ with alternating signs, leading to a Néel-like spin-density pattern and nonvanishing interactions between clusters, $E_{\mathrm{HF}(3)} = -1.1284Q$. We note in passing that for $s = 1$ and even q, all clusters have the same $m_i = 0$ state in HF, but $s_i \neq 0$, and the intercluster interaction is nonzero; for odd q, states alternate between $m_i = +1$ and $m_i = -1$.

Relative correlation energies p for cluster variants of UHF, SUHF, SGHF, and D_{Q}SGHF are plotted in Figure 4. Relative singlet-triplet gaps from SUHF, SGHF, D_{Q}SGHF, and ED are plotted in Figure 5. Numerical energy values are given for reference in Appendix C. The D_Q labels Γ for the ground states in sectors $S = 0$ and $S = 1$ depend on q, S, and N, as detailed in Table 1. (This information can be derived straightforwardly from the respective labels in D_N, which were given in Table III of [6]).

Table 1. Mulliken labels [a] of ground states in sectors $S = 0$ and $S = 1$ of even N antiferromagnetic $s = \frac{1}{2}$ rings in the reduced dihedral group D_Q ($Q = N/q$).

$N = 4n + 2$				$N = 4n$			
$S = 0$		$S = 1$		$S = 0$		$S = 1$	
q even	q odd	q even	q odd	q even	q odd	q even	q odd
A_2	B_1	A_1	A_1	A_1	A_1	A_2	B_1

[a] Label A(B) and subscript 1(2) respectively denote symmetry(antisymmetry) under the cyclic permutation $\hat{C}_Q$ or the vertical $\hat{C}_2$ operation that exchanges all sites pairwise.

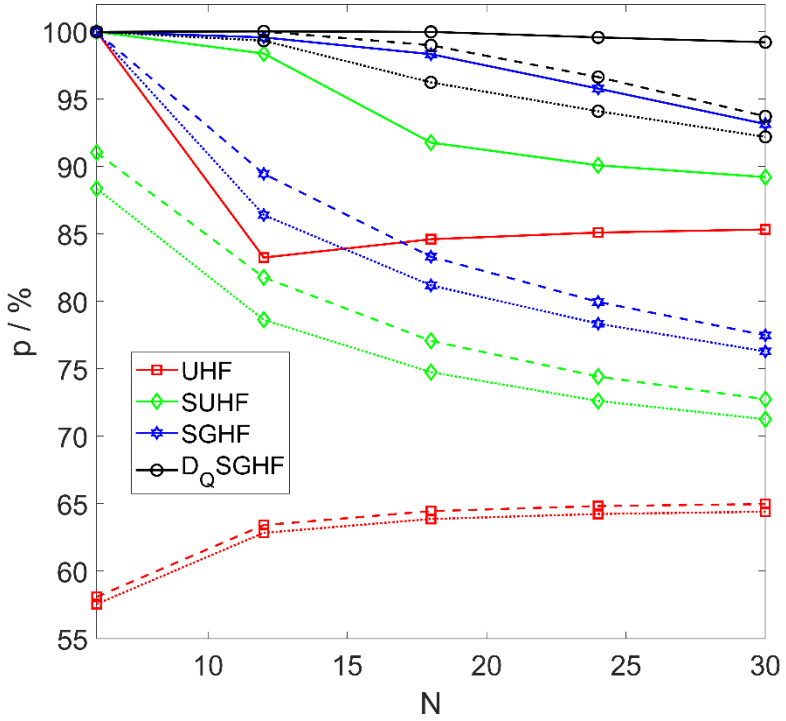

Figure 4. Relative correlation energies p (Equation (9)) from cluster variants of UHF, SUHF, SGHF and D_QSGHF ($Q = N/q$) in antiferromagnetic spin rings with $N = 6, 12, 18, 24, 30$ sites. Data points are connected by dotted (q = 2), dashed (q = 3) or solid lines (q = 6).

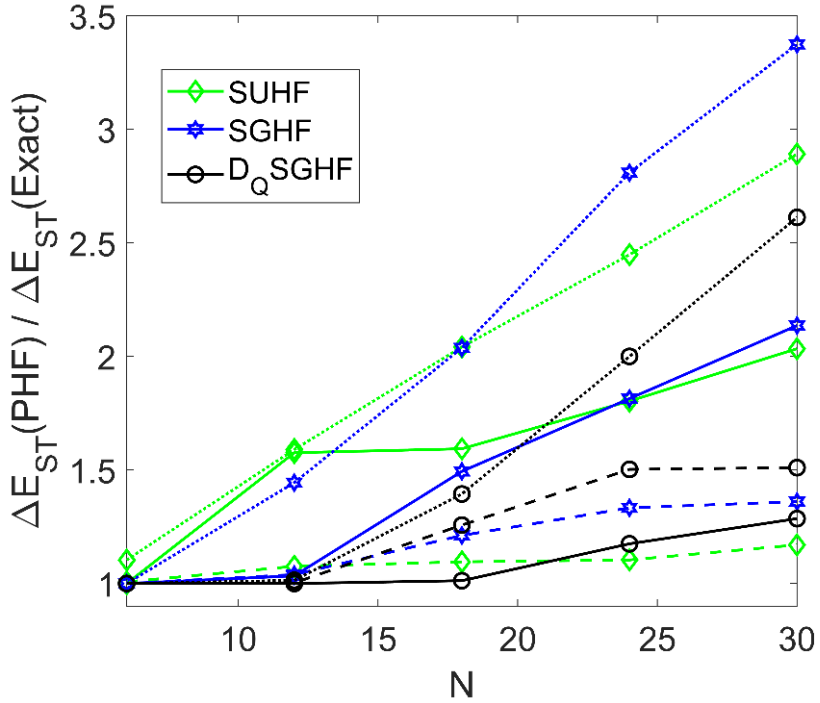

Figure 5. Relative singlet-triplet gaps from cluster variants of SUHF, SGHF and D_QSGHF ($Q = N/q$) in antiferromagnetic spin rings with $N = 6, 12, 18, 24, 30$ sites. Data points are connected by dotted (cluster size q = 2), dashed (q = 3) or solid lines (q = 6).

For $q = 2$ or $q = 6$, all clusters are $m_i = 0$ in the SUHF references for $S = 0$ or $S = 1$ projection. The fact that $S = 0$ energies are lower than UHF shows that SUHF does not yield a singlet-product. For a given state, system, and q, the ordering $E_{\mathrm{UHF}} \geq E_{\mathrm{SUHF}} \geq E_{\mathrm{SGHF}} \geq$

E_{PGSGHF} reflects the breaking and restoration of additional symmetries. (In contrast, in the absence of a group/subgroup relation between cPHF variants, such as in the set SGHF, PGGHF, or PGSUHF, it is not possible to determine the ordering a priori.) The equality holds only when the lower-level method is exact. This applies to $q = 6$, $N = 6$, where UHF (and any PHF variant) is trivially exact, as well as in a few other cases, e.g., SGHF(2) yields the numerically exact $S = 0$ and $S = 1$ ground states for $N = 6$.

For $q = 2$ or $q = 3$, an SUHF or SGHF wave function can be trivially expressed in the $q = 6$ basis. Thus, $q = 6$ will yield the best variational energy. In contrast, if D_Q-projection is included or if the larger cluster size is not a multiple of the smaller size we cannot rigorously predict if a larger q is advantageous. However, Figure 4 shows that this is indeed true in all studied cases. Excluding the exact $q = 6$, $N = 6$ point, the relative correlation p captured by UHF increases with N because rings with even N approach the Bethe–Hulthén limit $\lim_{N\to\infty} E/N = \frac{1}{4} - \ln 2$ from below [31]. With $E_{\mathrm{HF}}/N = -\frac{1}{4}$, the limits for cHF in Equations (11)–(13),

$$\lim_{N\to\infty} p_{\mathrm{UHF}(2)} = (\frac{1}{4} - \frac{3/4}{2})/(\frac{1}{2} - \ln 2) \approx 64.7\% \tag{11}$$

$$\lim_{N\to\infty} p_{\mathrm{UHF}(3)} \approx (\frac{1}{4} - \frac{1.1284}{3})/(\frac{1}{2} - \ln 2) \approx 65.3\% \tag{12}$$

$$\lim_{N\to\infty} p_{\mathrm{UHF}(6)} \approx (\frac{1}{4} - \frac{2.4936}{6})/(\frac{1}{2} - \ln 2) \approx 85.7\% \tag{13}$$

also hold for cPHF due to the lack of size extensivity (see Introduction). This limitation of cPHF is clearly apparent from the fact that p decreases with increasing N (Figure 4), but the improvement over ordinary PHF (where $\lim_{N\to\infty} p = 0$ for $q = 1$) is still significant. For example, for $N = 30$, $D_{30}\mathrm{SGHF}(1)$ ($N_{\mathrm{var}} = 60$) yields $E = -11.814$ [6] versus $E = -13.276$ with $D_5\mathrm{SGHF}(6)$ ($N_{\mathrm{var}} = 630$). Finally, $E = -13.320$ from $D_3\mathrm{SGHF}(10)$ ($N_{\mathrm{var}} = 6138$; not included in Figure 1) is very close to $E_0 = -13.322$ [32].

Triplet energies improve along the same hierarchy as singlet energies, but this does not guarantee an improvement in the gap ΔE_{ST}. Somewhat unfortunately, ΔE_{ST} is severely overestimated, except for small N and large q. The cluster approach can still afford better results than ordinary PHF. For example, for $N = 30$, $D_{30}\mathrm{SGHF}(1)$ yields $\Delta E_{\mathrm{ST}} = 0.212$ [6], compared to $\Delta E_{\mathrm{ST}} = 0.189$ from $D_5\mathrm{SGHF}(6)$ and an exact value of $\Delta E_{\mathrm{ST}} = 0.147$ [32].

3.2. Honeycomb Lattice Fragments

Systems with the connectivity of polycyclic aromatic hydrocarbons—triphenylene ($N = 18$), coronene (N = 24), hexabenzocoronene (N = 42), hexa-*cata*-hexabenzocoronene (N = 48), and kekulene (N = 48)—allow us to briefly explore options for cluster formation (the chemical nomenclature for these systems is not meant to imply that the Heisenberg model describes properties of the respective organic molecules). The lattices are bipartite [33] and thus have S = 0 ground states. For $s = \frac{1}{2}$ and up to eight different groupings (Figures 6–10; in some cases, the clusters are obviously not all equivalent), Table 2 compares energies from cUHF, cPHF, and cPT2 to exact results (available only for N = 18, 24).

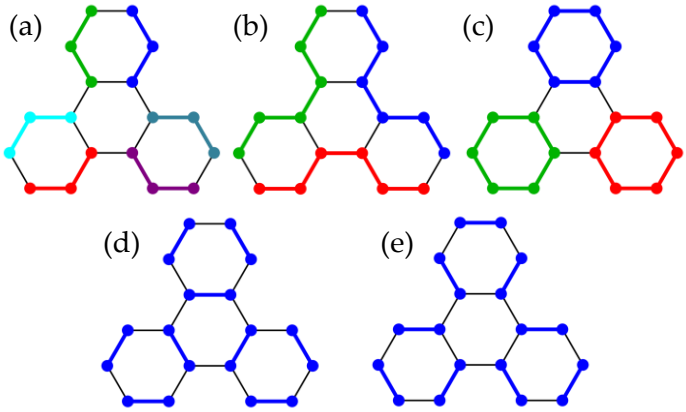

Figure 6. Cluster groupings in triphenylene $(N = 18)$ conserving the full D_3 symmetry. In (**a**–**c**), clusters are shown in different colors; in (**d**,**e**), all dimer clusters $(q = 2)$ are shown in the same color for simplicity.

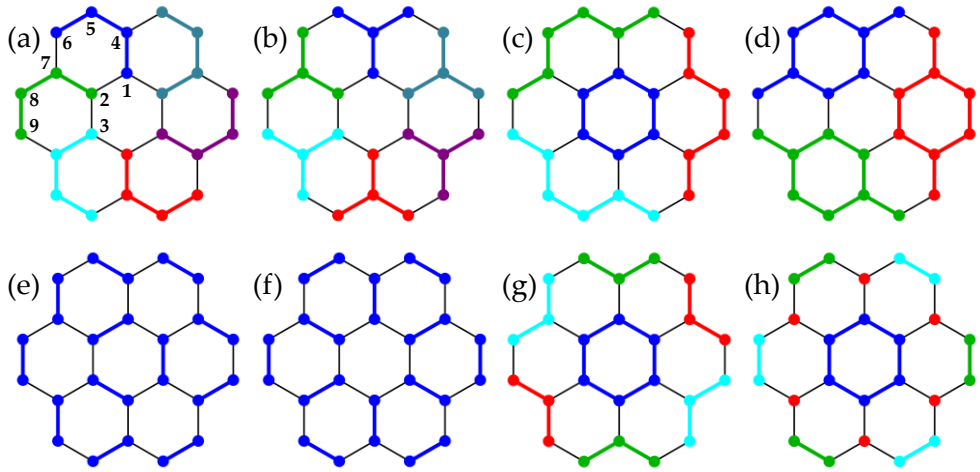

Figure 7. Cluster groupings in triphenylene ($N = 24$) with symmetries C_6 (**a**), D_6 (**b**,**f**–**h**), and D_3 (**c**–**e**). In (**e**,**f**), all dimers ($q = 2$) are shown in the same color for simplicity. In (**g**), three clusters comprise two separate trimers each. In (**h**), two clusters comprise three separate dimers, and six disconnected sites (red) constitute another cluster.

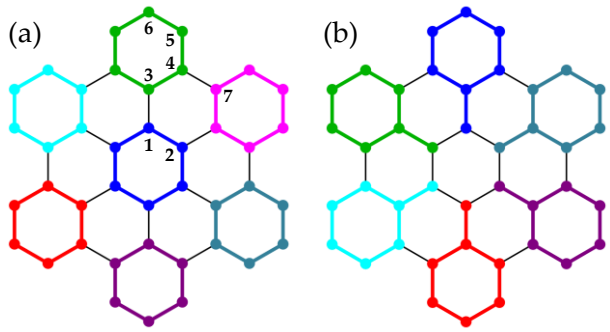

Figure 8. Cluster groupings ((**a**), $q = 6$) and ((**b**), $q = 7$) in hexabenzocoronene ($N = 42$) conserving the full D_6 symmetry.

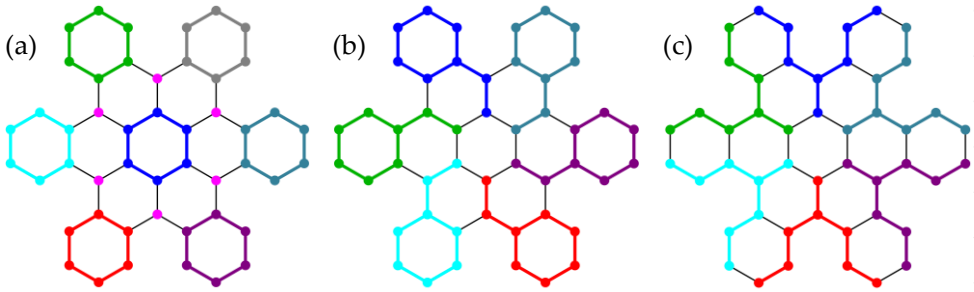

Figure 9. Cluster groupings in hexa-*cata*-hexabenzocoronene ($N = 48$) have symmetries D_6 (**a**,**c**) or C_6 (**b**). In (**a**), six disconnected sites (pink) constitute one cluster.

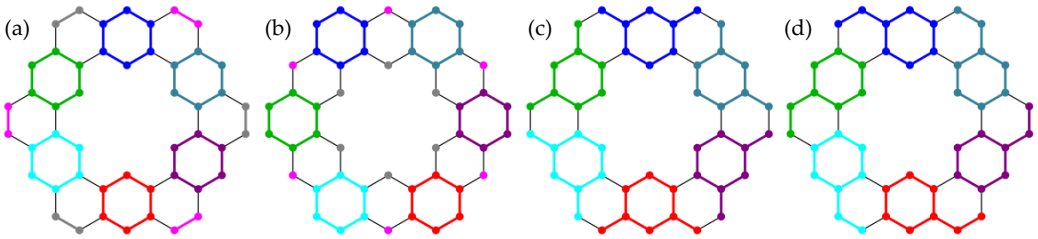

Figure 10. Cluster groupings in kekulene ($N = 48$) with symmetries D_3 (**a**), D_6 (**b**,**c**), and C_6 (**d**). In (**a**,**b**), two clusters (grey and pink) each comprise three separate dimers (**a**) or six separate sites (**b**).

Table 2. Ground-state energy estimates for honeycomb-lattice fragments from cluster variants of UHF, SGHF, PGSGHF, and PT2. The lowest energy for each grouping/method is given in bold type.

System	Grouping (q, Bonds) [a]	UHF	SGHF	PGSGHF (Γ)	PT2	Exact
Triphenylene	a (3, 12)	−7.2753	−8.2062	−8.6556 (A_2)	−8.6445	−8.7697
	b (6, 15)	−7.5804	−8.4865	−8.7342 (A_2)	−7.8205	
	c (6, 18)	**−8.4083**	**−8.7556**	**−8.7696** (A_2)	**−8.6640**	
	d (2, 9)	−7.0229	−8.0255	−8.5364 (A_2)	−8.2068	
	e (2, 9)	−6.9584	−7.8672	−8.4093 (A_2)	−8.1914	
Coronene	a (4, 24)	−10.2764	−11.2733	−11.7966 (A)	−11.4628	−11.9755
	b (4, 18)	−9.7660	−10.7447	−11.6399 (A_1)	−11.3781	
	c (6, 21)	−10.5736	−11.3457	−11.8103 (A_1)	−11.3740	
	d (8, 24)	**−10.8304**	**−11.6961**	**−11.9459** (A_1)	**−11.4992**	
	e (2, 12)	−9.5702	−10.6676	−11.2997 (A_1)	−11.3109	
	f (2, 12)	−9.6055	−10.7084	−11.6190 (A_1)	−11.3968	
	g (6, 18)	−9.9867	−10.9182	−11.6693 (A_1)	−11.1837	
	h (6, 12)	−9.4117	−11.1230	−11.8635 (A_1)	−11.1287	
Hexabenzo-coronene	a (6, 42)	**−19.8044**	−20.4297	−21.0044 (B_1)	−20.7082	– [b]
	b (7, 42)	−19.6337	**−20.4824**	**−21.0786** (B_1)	**−20.7724**	
Hexa-*cata*-hexabenzo-coronene	a (6, 42)	−21.5999	−23.0983	**−23.8296** (A_1)	−23.1753	– [b]
	b (8, 48)	**−22.4271**	**−23.3169**	−23.7980 (A)	**−23.4848**	
	c (8, 42)	−21.1057	−21.9885	−23.0109 (A_1)	−23.0836	
Kekulene	a (6, 48)	−21.4983	−22.2249	−22.7387 (A_1)	−22.9403	– [b]
	b (6, 36)	−19.8349	−20.9791	−22.4499 (A_1)	−22.2943	
	c (8, 48)	−21.4735	−22.2083	−23.0747 (A_1)	−22.9187	
	d (8, 48)	**−22.1306**	**−22.7459**	**−23.3603** (A)	**−23.2404**	

[a] Labels refer to Figures 6–10; cluster size q and the number of intracluster bonds are given in parentheses. [b] System size exceeds our ED capabilities.

In triphenylene, grouping (b) is obtained from (a) by merging clusters, while conserving the full PG-symmetry, and (b) is thus guaranteed to yield lower cPHF energies than (a). The same is true for (c) with respect to the two complementary dimer formations (d) and (e). In fact, D_3SGHF(6) based on (c) with three benzene units, each hosting a Clar sextet in the most favorable resonance structure [34], is very close to the exact ground state.

In coronene, grouping (d), including 24 of 30 bonds in the clusters, is obtained from (b) by merging neighboring clusters pairwise and recovers 99.75% of E_0 with D_3SGHF(8). For cluster types (a)–(d), Table 3 collects all distinct nearest-neighbor (NN) and a few next-nearest neighbor (NNN) SPCFs. Their magnitude is generally somewhat over- or underestimated (with minor exceptions), depending on whether sites reside in the same (bold type in Table 3) or in different clusters, respectively. It thus appears generally advantageous to include pairs of strongly antiferromagnetically correlated sites in a cluster. The SPCFs evidence a moderate degree of spatial-symmetry breaking, $D_6 \to C_6$ in (a), $D_6 \to D_3$ in (c), and $D_6 \to D_3$ in (d), but not in (b), because this grouping allows full D_6-projection.

Table 3. SPCFs $\left\langle \hat{\mathbf{s}}_i \cdot \hat{\mathbf{s}}_j \right\rangle$ in coronene from PGSGHF, compared against exact results. Letters (a, b, c, d) identifying cluster groupings, and the site numbers (first column) are defined in Figure 7 [a].

i–j	C_6**SGHF(4) (a)**	D_6**SGHF(4)(b)**	D_3**SGHF(6) (c)**	D_3**SGHF(8) (d)**	**Exact**
1–2	−0.33729	−0.35059	**−0.39063**	**−0.36850**	−0.35875
2–3	−0.33729	−0.35059	**−0.38706**	−0.33627	−0.35875
1–4	**−0.40404**	**−0.35322**	−0.30621	**−0.37926**	−0.37507
4–5	**−0.37034**	**−0.40476**	**−0.37196**	**−0.37095**	−0.36665
5–6	**−0.54911**	−0.42665	**−0.52422**	**−0.52685**	−0.52881
6–7	−0.30533	**−0.40476**	**−0.37196**	**−0.37095**	−0.36665
7–8	**−0.37034**	**−0.40476**	**−0.41287**	**−0.36483**	−0.36665
8–9	**−0.54911**	−0.42665	−0.45278	−0.52027	−0.52881
(1–3)	0.17744	0.19472	**0.19503**	0.16792	0.16641
(1–5)	**0.18265**	**0.20098**	0.16410	**0.17971**	0.17661
(2–6)	0.18009	**0.20098**	0.16410	**0.17971**	0.17661
(4–6)	**0.20777**	0.18967	**0.19643**	**0.19440**	0.19291
(5–7)	0.17515	0.18967	**0.19643**	**0.19440**	0.19291

[a] SPCFs for all distinct NN pairs *i–j* (first column) are given, including pairs that are equivalent in the full symmetry group but inequivalent in some of the PGSGHF wave functions. The NNN set (pairs *i–j* in parentheses) is not complete, except for (b), which maintains the full D_6 symmetry. Bold type is used for SPCFs of pairs that belong to the same cluster.

Due to computational limitations, we cannot carry out ED on the $N = 42$ and $N = 48$ lattices, but a comparison with cPT2 suggests that cPHF is still fairly accurate in these larger systems. In hexabenzocoronene, both options include a fraction of 42/54 bonds in the clusters. Although $q = 6$ (Figure 8a) has seven intact rings, and thus loosely corresponds to the most favorable resonance structure with seven Clar sextets [34], $q = 7$ (Figure 8b) with six sextets is energetically very slightly favored in D_6SGHF, though not in UHF (Table 2). In hexa-*cata*-hexabenzocoronene, D_6SGHF(6) with 42/60 bonds in seven rings (Figure 9a) yields a significantly lower energy than D_6SGHF(8) with the same number of intracluster bonds but no intact rings (Figure 9c) and is even slightly better than C_6SGHF(8) with 48 intracluster bonds but only six rings (Figure 9b). Finally, in kekulene, grouping (d) predicts the lowest energy, despite $D_6 \to C_6$ symmetry breaking. In contrast to (a), (c), and (d), the six Clar sextets are broken up in (b), which features only 36/60 bonds and yields higher energies in cHF, cPHF, and cPT2.

3.3. Polyhedra

We lastly consider four polyhedra (Figure 11) with T_d or I_h symmetry, which allow cluster groupings that fully respect spatial symmetry.

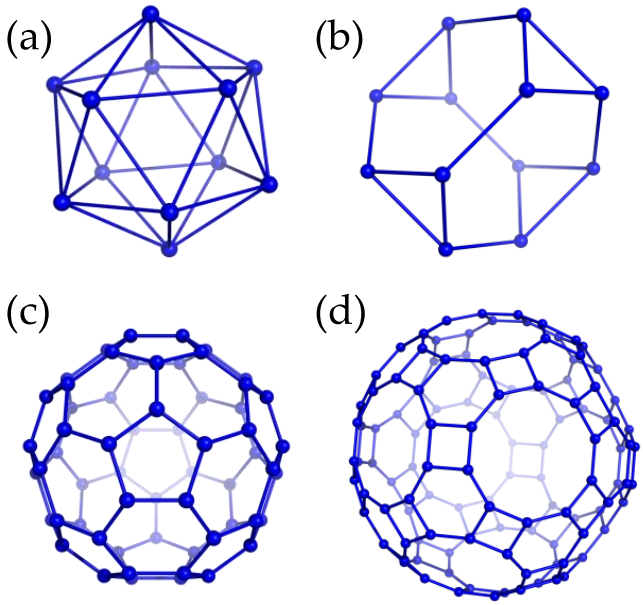

Figure 11. Icosahedron (**a**), truncated tetrahedron (**b**), truncated icosahedron (**c**), and truncated icosidodecahedron (**d**).

(a) Icosahedron

Dimers of the sites related by spatial inversion C_i conserve I_h symmetry (Figure 12a), while nearest-neighbor pairs break symmetry (D_{2h}, Figure 12b), as do hexamers (D_{5d}, Figure 12c). For $s > \frac{1}{2}$, the antiferromagnetic spin-pair correlation $\langle \hat{\mathbf{s}}_1 \cdot \hat{\mathbf{s}}_4 \rangle$ between the most distant sites (numbers defined in Figure 12a) exceeds the NN correlation $\langle \hat{\mathbf{s}}_1 \cdot \hat{\mathbf{s}}_2 \rangle$ in the exact wave functions, see Table 4.

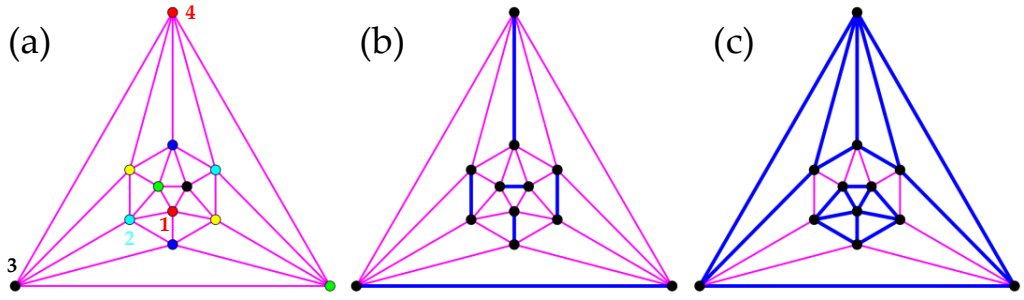

Figure 12. Three cluster groupings in the icosahedron conserve I_h ((**a**), $q = 2$), D_{2h} ((**b**), $q = 2$), or D_{5d} symmetry ((**c**), $q = 6$). In the planar projections (Schlegel diagrams), interacting sites belonging to the same or to different clusters are connected by blue or pink lines, respectively. In (**a**), the color of sites assigns them to one of six clusters. Sites forming symmetry-inequivalent pairs with site 1 are numbered in (**a**).

Table 4. Comparison of I_hSGHF(2) predictions of SPCFs in the ground state of the icosahedron with $\frac{1}{2} \leq s \leq 2$ against exact values. Site numbers are defined in Figure 12a.

s		$\langle \hat{\mathbf{s}}_1 \cdot \hat{\mathbf{s}}_2 \rangle$	$\langle \hat{\mathbf{s}}_1 \cdot \hat{\mathbf{s}}_3 \rangle$	$\langle \hat{\mathbf{s}}_1 \cdot \hat{\mathbf{s}}_4 \rangle$
1/2	Exact	−0.2063	0.0841	−0.1397
	PHF	−0.2063	0.0841	−0.1397
1	Exact	−0.6187	0.3680	−0.7463
	PHF	−0.6187	0.3680	−0.7464
3/2	Exact	−1.2580	0.9060	−1.9899
	PHF	−1.2580	0.9062	−1.9910
2	Exact	−2.1237	1.6616	−3.6897
	PHF	−2.1236	1.6621	−3.6926

Interestingly, the I_h grouping (a) is advantageous over D_{2h} (b), see Table 5, except for GHF, where (a) yields the classical solution [35], while (b) profits energetically from correlation in the dimers. For $s = \frac{1}{2}$, GHF yields local singlets in (b), which are broken up in the SGHF reference, as apparent from the energy lowering, $E_{\mathrm{SGHF}} < E_{\mathrm{GHF}}$. For $s = \frac{1}{2}, 1, \frac{3}{2}, 2$, I_hSGHF(2) yields 100%, 99.999%, 99.996%, and 99.995%, respectively, of the exact ground-state energy and thereby recovers most of the correlation energy missing from I_hSGHF(1) [6]. Not surprisingly, SPCFs are very close to the exact results (Table 4), corroborating the high quality of the I_hSGHF(2) wave functions.

Table 5. GHF and PHF estimates of ground-state energies of the antiferromagnetic icosahedron with $\frac{1}{2} \leq s \leq 2$ for two different $q = 2$ groupings (Figure 12a,b) with I_h or D_{2h} symmetry.

s	Grouping	GHF	SGHF	PGSGHF	Exact (Γ)
1/2	D_{2h}	−4.5000	−5.3224	−6.1717	−6.1879 (Au)
	I_h	−3.3541	−5.7644	−6.1879 [a]	
1	D_{2h}	−14.3025	−17.4565	−18.1678	−18.5611 (Ag)
	I_h	−13.4164	−18.2225	−18.5609	
3/2	D_{2h}	−31.4256	−36.2633	−37.3073	−37.7412 (Au)
	I_h	−30.1869	−37.3842	−37.7396	
2	D_{2h}	−55.2658	−61.7751	−63.1481	−63.7104 (Ag)
	I_h	−53.6656	−63.2529	−63.7075	

[a] Exact ground-state energy within numerical double precision.

Incidentally, I_hGHF(2) (without explicit S-projection) converges onto the exact ground state of the $s = \frac{1}{2}$ system (the numerical deviation from E_0 is $\approx 10^{-15}$). In contrast, in I_hKGHF(1), the additional use of complex-conjugation symmetry (K) was required to reach the exact solution [6]. The fact that the exact ground state for $s = \frac{1}{2}$ is also obtained with D_{5d}SGHF(6) (Figure 12c) shows that a cluster grouping that breaks symmetry does not necessarily lead to a symmetry-broken cPHF wave function. SGHF(2) wave functions are totally symmetric in group I but have mixed symmetry under spatial inversion C_i ($I_h = I \otimes C_i$). For $s = \frac{1}{2}$, the respective weights in the SGHF(2) wave function are $w_{\mathrm{A_g}} \approx 0.418$ and $w_{\mathrm{A_u}} \approx 0.582$ ($w_{\mathrm{A_g}} + w_{\mathrm{A_u}} = 1$).

(b) Truncated Tetrahedron

The classical solution for the truncated tetrahedron [36] minimizes frustration on the four triangles (with angles of 120 between spins) and aligns spins on the bonds between triangles antiparallel. Two complementary cluster groupings defined by either six classically

unfrustrated bonds (u-bonds, $q = 2$, Figure 13a) or twelve frustrated bonds (f-bonds, $q = 3$, Figure 13b) maintain tetrahedral T_d symmetry.

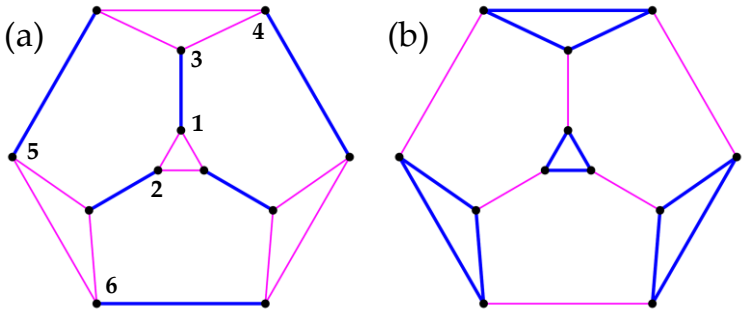

Figure 13. Dimers (**a**) and trimers (**b**) respect the full T_d symmetry of the truncated tetrahedron. For more details, see caption to Figure 12.

Table 6 shows that u-bonds $(q = 2)$ yield lower GHF and SGHF energies than f-bonds $(q = 3)$, despite a smaller number of variational parameters, e.g., for $s = 2$, $N_{\mathrm{var}} = 288$ for $q = 2$, and $N_{\mathrm{var}} = 992$ for $q = 3$. However, the larger variational freedom provided by f-bonds leads to slightly better energies for T_dSGHF(3) compared to T_dSGHF(2). The somewhat larger deviations between PGSGHF and exact results than in the icosahedron may be attributed to the lower order of the group ($h = 24$ in T_d versus $h = 120$ in I_h), although a direct comparison between these two polyhedra is not meaningful. For $q = 1$ [6] and $q = 2$, though not for $q = 3$, and for all tested values of s, the SGHF reference $|\Phi\rangle$ can be revealed to have the classical spin-density structure by appropriate gauge transformations [22]. (For additional comments on this issue, see the following section on the truncated icosahedron.) SGHF(1) [6] and SGHF(2) wave functions transform like the exact ground state (A_2 or A_1 for half-integer or integer s, respectively).

Table 6. GHF and PHF estimates of ground-state energies of the antiferromagnetic $\frac{1}{2} \leq s \leq 2$ truncated tetrahedron for two different groupings (Figure 13).

s	q	GHF	SGHF	T_dSGHF	Exact (Γ)
1/2	2	−4.5000	−5.2700	−5.7009 [a]	−5.7009 (A_2)
	3	−3.8881	−4.8147	−5.7009 [a]	
1	2	−14.0173	−16.0342	−17.1649	−17.1955 (A_1)
	3	−13.8696	−15.7195	−17.1775	
3/2	2	−29.7756	−32.8938	−34.4456	−34.6402 (A_2)
	3	−29.6977	−32.5614	−34.4796	
2	2	−51.5616	−55.7815	−57.7827	−58.1140 (A_1)
	3	−51.5327	−55.3924	−57.8181	

[a] Exact ground-state energy within numerical double precision.

(c) Truncated Icosahedron

In contrast to icosidodecahedral arrangements of spin centers in Keplerate molecules $\{Mo_{72}V_{30}\}$ [37,38], $\{W_{72}V_{30}\}$ [39], $\{Mo_{72}Cr_{30}\}$ [40], and $\{Mo_{72}Fe_{30}\}$ [41,42], with $s = \frac{1}{2}, \frac{3}{2}, \frac{5}{2}$ for V^{3+}, Cr^{3+}, Fe^{3+}, truncated icosahedra were not yet synthetically realized as magnetic molecules. The respective Heisenberg model was nevertheless addressed in a few works [29,43–49], some of which were motivated by gaining an understanding of the properties of buckminsterfullerene C_{60}. However, electronic-structure calculations have shown that the Heisenberg model is at best of qualitative value for C_{60} because this molecule possesses $\ll 60$ unpaired electrons [50] (but note that there is no unique measure for

this number). It was eventually concluded that C_{60} displays no significant strong correlation [51]. Ab initio GHF calculations [50] on C_{60} still reproduce the exotic three-dimensional spin-density pattern of the classical Heisenberg ground state [29]. Geometry optimization on the GHF level-of-theory yields a perfect I_h structure for C_{60} [50], but the spatial inversion C_i is the only obvious self-consistent symmetry of the GHF solution. We specify the hidden icosahedral symmetry I in Figure 14, where classical spin vectors are plotted in a Schlegel diagram. A uniform rotation was applied such that spins in the central pentagon in Figure 14 lie in the geometrical plane of that pentagon, with the spin on the first site pointing in the negative x-direction. This spin configuration is left unchanged by a combined spin rotation (R) by 144° and a five-fold site permutation (P). In the electronic-structure problem, the site permutation corresponds to a spatial rotation. These operations are performed about an axis through the coordinate origin (the center of the truncated icosahedron) and the center of the central pentagon (marked 5_{PR} in Figure 14).

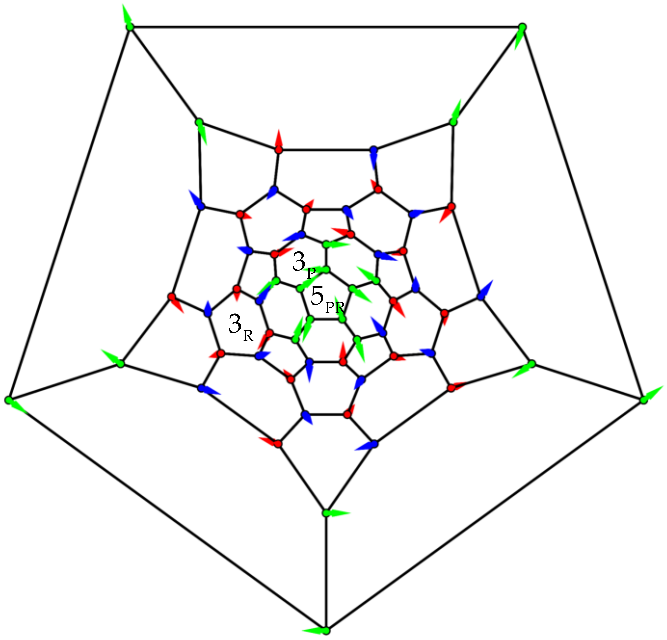

Figure 14. Classical three-dimensional spin configuration of the truncated icosahedron. Green spin vectors lie in the xy-plane (paper plane); red/blue vectors point in the negative/positive z-direction. The first vector on the central pentagon points in the (horizontal) negative x-direction. Symmetry elements ($3_P \times 3_R = 3_{PR}$, and 5_{PR}, see main text for details) are defined with respect to an axis through the coordinate origin and the center of the respective pentagon or hexagon.

A spin rotation by 120 about an axis through the midpoint of a hexagon (3_R, Figure 14), combined with a threefold site permutation about another hexagon (3_P) is a second symmetry $(3_P \times 3_R = 3_{PR})$, and 5_{PR} and 3_{PR} are generators of a group isomorphic to group I. The full symmetry group of the classical (or GHF) solution is $I_h = I \otimes C_i$. This overall explains why GHF orbitals of C_{60} are up to six-fold degenerate: molecular orbitals span irreducible representations [52] of the double group I_h^*.

Two complementary cluster formations preserve spatial I_h symmetry by including either the 30 u-bonds between pentagons (q = 2, Figure 15a) or the 60 f-bonds in the pentagons (q = 5, Figure 15b). Classical spins are antiparallel on u-bonds (see Figure 15a) and span angles of 144° on the f-bonds. We additionally consider fused hexagons (q = 10, Figure 15c), thereby including 36 f-bonds and all 30 u-bonds in the clusters and reducing symmetry, $I_h \to D_{2h}$.

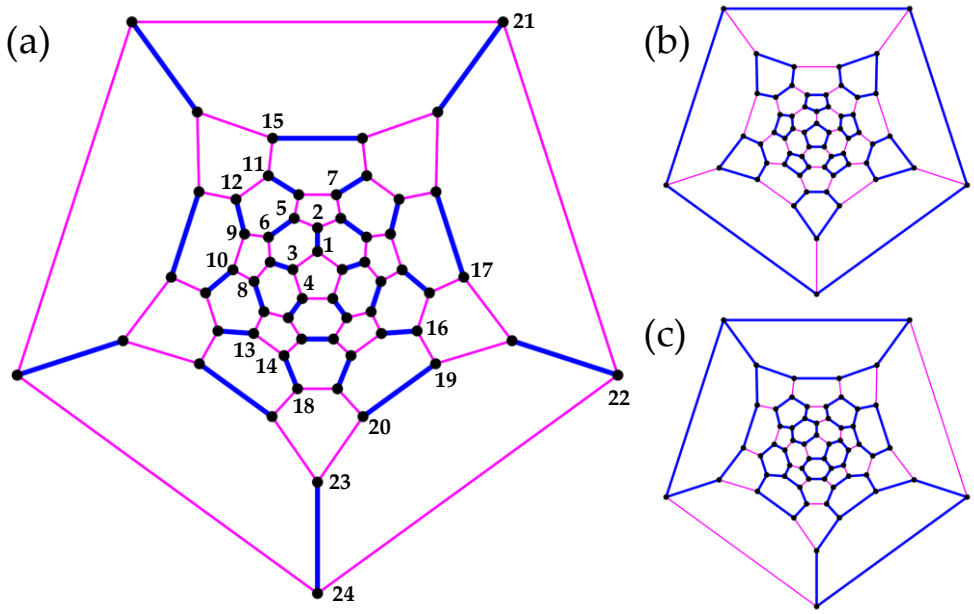

Figure 15. Interpentagon bonds ((**a**), $q = 2$) or pentagon clusters ((**b**), $q = 5$) maintain the I_h symmetry of the truncated icosahedron. Fused hexagons ((**c**), $q = 10$) reduce symmetry to D_{2h}. The numbering (**a**) of centers forming inequivalent pairs with site 1 follows Figure 3 in [43].

Interestingly, GHF(2) can be solved analytically for $s = \frac{1}{2}$. Starting from the classical solution [29], $E_{\mathrm{HF}} = -\frac{15}{4}(3+\sqrt{5}) \approx -19.6353$, we define a u-bond wave function $|\Phi_i\rangle$ in Equation (14),

$$|\Phi_i\rangle = \frac{1}{\sqrt{1+\alpha^2}}(|\uparrow\downarrow\rangle + \alpha|\downarrow\uparrow\rangle) \tag{14}$$

that depends on a real parameter α. The local quantization axis for projections $\uparrow$ and $\downarrow$ in a cluster i are given by the classical solution, that is, $\alpha = 0$ recovers GHF(1). Thus, all spins retain their classical orientation in GHF(2), but Equation (14) allows the local singlet to acquire a higher weight than the triplet. Each dimer contributes an energy λ, as shown in Equation (15):

$$\lambda = \langle\Phi_i|\hat{\mathbf{s}}_1 \cdot \hat{\mathbf{s}}_2|\Phi_i\rangle = \frac{1}{1+\alpha^2}\left(-\frac{\alpha^2}{4} + \alpha - \frac{1}{4}\right). \tag{15}$$

Compared to GHF(1), the local magnetization $|\langle\hat{\mathbf{s}}_m\rangle|$ is reduced by a factor κ, Equation (16), in the GHF(2) wave function.

$$\kappa = \frac{1-\alpha^2}{1+\alpha^2} \tag{16}$$

Interactions along the intercluster bonds (f-bonds) are evaluated classically,

$$\langle\hat{\mathbf{s}}_m \cdot \hat{\mathbf{s}}_n\rangle = \langle\hat{\mathbf{s}}_m\rangle \cdot \langle\hat{\mathbf{s}}_n\rangle = \left(\frac{\kappa}{2}\right)^2 \cos\phi\,, \tag{17}$$

with $\phi = \frac{4\pi}{5}$ (144°). Minimization of the total GHF(2) energy E, Equation (18),

$$E = 30\lambda + 60\left(\frac{\kappa}{2}\right)^2 \cos\left(\frac{4\pi}{5}\right), \tag{18}$$

with respect to α, affords α_{opt} in Equation (19),

$$\alpha_{\mathrm{opt}} = -\frac{1}{4}\left[\left(1+\sqrt{5}\right)\left(2+\sqrt{2}\sqrt{\sqrt{5}-1}\right)\right], \tag{19}$$

corresponding to κ_{opt} in Equation (20),

$$\kappa_{\text{opt}} = \left| \frac{1-\alpha_{\text{opt}}^2}{1+\alpha_{\text{opt}}^2} \right| = \sqrt{\frac{\sqrt{5}-1}{2}}\,, \tag{20}$$

and overall results in Equation (21),

$$E_{\text{GHF(2)}} = -\frac{15}{2}\left(1+\sqrt{5}\right) \approx -24.2705\,. \tag{21}$$

Numerical calculations indeed converge onto this solution. (An analogous analysis for the $s = \frac{1}{2}$ truncated tetrahedron yields $\alpha_{\text{opt}} = 1$, that is, singlets are formed on the six u-bonds.) GHF(2) significantly improves over GHF(1) but still falls short of an accurate description. Other works derived the following variational estimates for the $S = 0$ ground state: $E = -29.97$ [45] (resonating valence-bond, RVB), $E = -30.83$ [44], or $E = -30.69$ [43] (Variational Monte Carlo with a Gutzwiller projector, VMC), and $E = -31.13$ [47] (DMRG). The latter most recent result (DMRG) may be regarded as a quasiexact benchmark value. The GHF and PHF energies ($q = 2, 5, 10$) are collected in Table 7. Our best estimate of $E = -29.98$, obtained with D_{2h}SGHF(10), is very close to the RVB result [45] and corresponds to p = 90%. In view of the Hilbert-space dimension of $\mathcal{N} = 2^{60} \approx 10^{18}$, which is presently still infeasible for ED, even if symmetries were employed to reduce the matrix size, we would like to emphasize the very significant state-space reduction afforded by cPHF in terms of $N_{\text{var}} = 180$ for q = 2, $N_{\text{var}} = 744$ for q = 5, and $N_{\text{var}} = 12276$ for q = 10.

Table 7. cGHF and cPHF estimates of ground-state energies of the $s = \frac{1}{2}$ truncated icosahedron.

q	GHF	SGHF	PGSGHF [a]
2	−24.2705	−25.5486	−27.8429
5	−25.8525	−26.6072	−28.5653
10	−28.6199 [b]	−29.2195	−29.9842

[a] Projection onto $S = 0, \Gamma = \text{A}_\text{g}$. [b] All clusters assume their local singlet ground state.

As explained, GHF(2) spin densities (local magnetizations) maintain the classical structure. Our numerical calculations showed that this also holds true for GHF(5). Although SGHF(2) or SGHF(5) will generally converge onto a reference $|\Phi\rangle$ that does not display the classical spin-density pattern, we found that the latter can be restituted by gauge rotations on $|\Phi\rangle$ that leave the S-projected state $\hat{P}_0^0|\Phi\rangle$ unchanged (redundancies in the definition of $|\Phi\rangle$ with respect to gauge transformations related to spin symmetry were discussed in [22]): $|\Phi\rangle$ assumes the classical magnetization pattern when it is ensured through appropriate gauge transformations that the expectation value of the total-spin vector vanishes, $\langle\Phi|\hat{\mathbf{S}}|\Phi\rangle = \mathbf{0}$. Irrespective of whether such transformations are applied to $|\Phi\rangle$, SGHF(2) and SGHF(5) wave functions (S = 0) have pure A_g symmetry in I_h. For $q = 1$, $|\Phi_{\text{HF}}\rangle$ is the optimal reference for $S = 0$ projection in SGHF ($E_{\text{SGHF(1)}} = -21.6515$), which appears to be a rather general feature of highly symmetric polyhedra [6] but is not true for spin rings [6] or for the presently studied polyhedra if $q > 1$. In other words, for $q > 1$, the variation-after-projection (VAP) approach of SGHF is not equivalent to a far simpler projection-after-variation (PAV) "single-shot" S-projection of $|\Phi_{\text{HF}}\rangle$.

In Table 8, PHF predictions for SPCFs from SGHF and I_hSGHF ($q = 2, 5$) are compared to VMC [43]. Note that the energy of a variational trial function that respects icosahedral symmetry is $E = 30\langle\hat{\mathbf{s}}_1 \cdot \hat{\mathbf{s}}_2\rangle + 60\langle\hat{\mathbf{s}}_1 \cdot \hat{\mathbf{s}}_3\rangle$. The magnitude of the antiferromagnetic u-bond correlation $\langle\hat{\mathbf{s}}_1 \cdot \hat{\mathbf{s}}_2\rangle$ is underestimated by I_hSGHF(5), while the magnitude of $\langle\hat{\mathbf{s}}_1 \cdot \hat{\mathbf{s}}_3\rangle$ in the f-bonds is overestimated. The reverse is true for I_hSGHF(2), which yields $\langle\hat{\mathbf{s}}_1 \cdot \hat{\mathbf{s}}_2\rangle$ and $\langle\hat{\mathbf{s}}_1 \cdot \hat{\mathbf{s}}_3\rangle$ values that match the VMC estimates more closely. This further illustrates the trend observed in the hexagonal lattices of over- or underestimating correlations in intra-

or intercluster bonds, respectively. Except for I_hSGHF(2), cPHF overestimates long-range correlation rather dramatically.

Table 8. SPCFs, $\left\langle \hat{\mathbf{s}}_1 \cdot \hat{\mathbf{s}}_j \right\rangle$, for all distinct pair types (numbering defined in Figure 15) in the ground state of the truncated icosahedron. VMC results were taken from Table II in [43].

	$q = 2$		$q = 5$		
E	−25.5486	−27.8429	−26.6072	−28.5653	−30.69
j	SGHF	I_hSGHF	SGHF	I_hSGHF	VMC
2	−0.562	−0.610	−0.186	−0.277	−0.529
3	−0.145	−0.159	−0.351	−0.337	−0.247
4	0.051	0.051	0.076	0.073	0.030
5	0.136	0.137	0.142	0.154	0.141
6	−0.145	−0.154	−0.151	−0.154	−0.142
7	−0.056	−0.054	−0.059	−0.061	−0.023
8	−0.090	−0.080	−0.094	−0.093	−0.038
9	0.084	0.070	0.087	0.083	0.031
10	−0.002	0.001	−0.003	−0.001	0.001
11	0.051	0.049	0.052	0.051	0.027
12	−0.090	−0.072	−0.094	−0.088	−0.026
13	−0.090	−0.042	−0.094	−0.084	−0.002
14	0.051	0.017	0.052	0.046	−0.001
15	−0.002	−0.002	−0.003	−0.003	−0.004
16	0.084	0.037	0.087	0.078	0.001
17	−0.090	−0.036	−0.094	−0.081	0.002
18	−0.056	−0.018	−0.059	−0.051	0.013
19	−0.145	−0.042	−0.151	−0.129	0.000
20	0.136	0.039	0.142	0.124	−0.002
21	0.051	0.016	0.053	0.046	−0.030
22	−0.145	−0.040	−0.150	−0.128	0.007
23	−0.179	−0.046	−0.186	−0.158	0.016
24	0.168	0.044	0.176	0.152	−0.008

We are not aware of any previous works addressing ground states in the truncated icosahedron with $s > \frac{1}{2}$. For $\frac{1}{2} \leq s \leq 2$, energies from GHF, SGHF, and I_hSGHF ($q = 2$) are collected in Table 9, where they are compared with local singlets on fused benzene rings ($q = 10$) and with PT2(1) and PT2(2). Except for $s = \frac{1}{2}$, where the singlet-product represents the GHF(10) solution, I_hSGHF yields the best variational energy. For the $s = \frac{1}{2}$ system, the PT2(1) energy, $E = -31.05$ [29], is incidentally rather close to the DMRG result, $E = -31.13$ [47], but the PT2(2) prediction deviates significantly, $E = -29.12$.

The relative deviation between PT2 energies and I_hSGHF is smallest for $s = 2$. The Hilbert-space of dimension $\mathcal{N} = 5^{60} \approx 9 \times 10^{41}$ for $s = 2$ is completely out of reach of ED. The problem size is again drastically reduced by cPHF(2), which operates with merely $N_{\text{var}} = 1440$ variational parameters. Somewhat unfortunately, we cannot offer a reliable assessment of the accuracy of cPHF in this rather large system, where obtaining an accurate reference value with DMRG would be very challenging.

Table 9. Variational estimates from GHF; SGHF; I_hSGHF (projection onto $S = 0$, $\Gamma = A_g$), a singlet-product on fused hexagons ($q = 10$); and PT2 for the ground state of the truncated icosahedron with $\frac{1}{2} \leq s \leq 2$.

s	GHF (2)	SGHF (2)	I_hSGHF (2)	q = 10, s_i = 0	PT2 (1)	PT2 (2)
1/2	−24.2705	−25.5486	−27.8429	−28.6199	−31.0543	−29.1216
1	−85.6371	−87.7764	−90.1147	−89.8943	−96.7113	−96.9910
3/2	−186.6961	−189.5706	−192.4293	−183.7630	−202.2428	−203.7112
2	−327.0802	−330.4438	−343.1173	−310.5941	−347.1526	−349.5852

(d) Truncated icosidodecahedron

Lastly, as another demonstration of the applicability of cPHF to systems that are far too large for ED, we consider a truncated icosidodecahedron with 120 $s = \frac{1}{2}$ vertices, $\mathcal{N} = 2^{120} \approx 10^{36}$.Figure 16 presents three symmetry-compatible cluster groupings ($q = 4, 6, 10$).

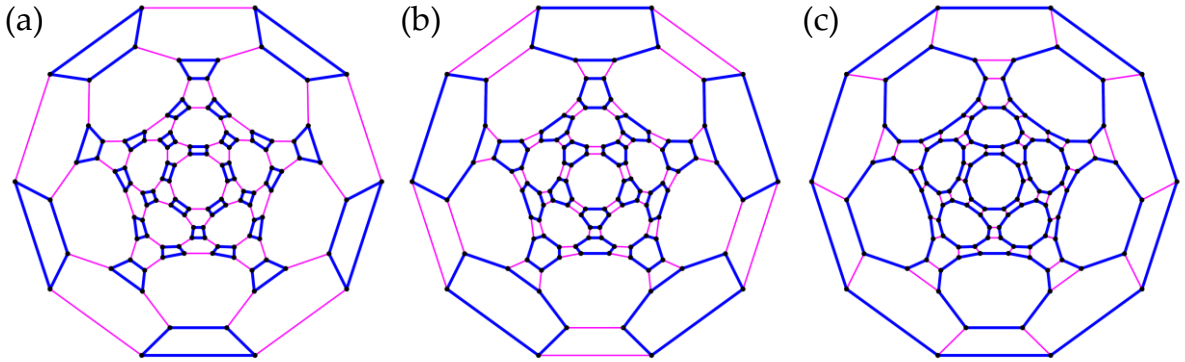

Figure 16. Cluster groupings compatible with I_h symmetry in the truncated icosidodecahedron. The midpoints of the squares ((**a**), $q = 4$), hexagons ((**b**), $q = 6$), and decagons ((**c**), q = 10) form an icosidodecahedron (Q = 30), dodecahedron (Q = 20), or icosahedron (Q = 12), respectively.

Being bipartite, the system has a nondegenerate $S = 0$ ground state, which should transform as A_g (like the classical Néel state, $E_{\mathrm{UHF}(1)} = -45$). With 120/180 bonds included in the clusters, none of the three groupings has an obvious advantage: $E_{\mathrm{UHF}(4)} = -60.7642$, $E_{\mathrm{UHF}(6)} = -59.0690$, $E_{\mathrm{UHF}(10)} = -58.8657$. For a given q, all clusters assume the same $m_i = 0$ state, but no local singlets are formed ($s_i \neq 0$), leading to spin densities of Néel-type. We selected $q = 4$ for cPHF calculations ($N_{\mathrm{var}} = 900$) : $E_{\mathrm{SUHF}} = -61.3769$, $E_{\mathrm{SGHF}} = -61.6502$, $E_{I_h\mathrm{SGHF}} = -64.0101$. With respect to I_hSGHF, q = 6 ($N_{\mathrm{var}} = 2520$) is still inferior to q = 4, yielding $E_{I_h\mathrm{SGHF}} = -62.7728$. The same trend is true for PT2: $E_{\mathrm{PT2}(4)} = -64.9139$, $E_{\mathrm{PT2}(6)} = -64.0437$.

SPCFs (referring to the site numbering of Figure 17) from $I_h\mathrm{SGHF}(4)$ are plotted in Figure 18. All correlations within the same sublattice are positive; all correlations between different sublattices are negative. The strong correlation across the whole range of the molecule is most likely artifactual, because PHF (or cPHF) reverts to HF (or cHF) in the thermodynamic limit [5,6]. Therefore, long-range order for large systems is generally exaggerated.

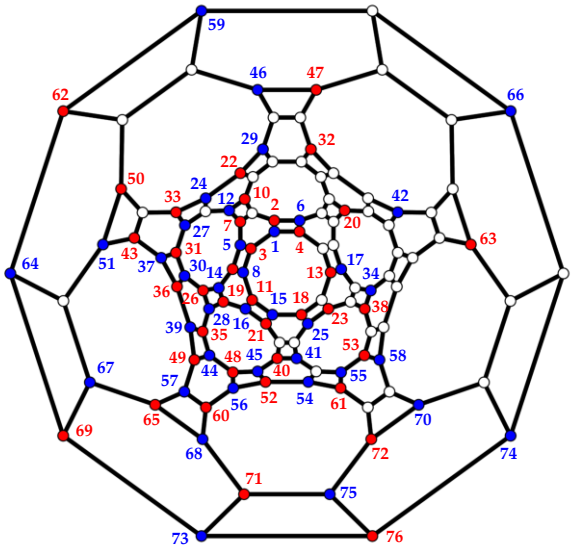

Figure 17. Numbering of centers forming inequivalent pairs with site 1 in the bicolorable (red, blue) truncated icosidodecahedron lattice. Sites without a number are white but still belong to one of the two sublattices.

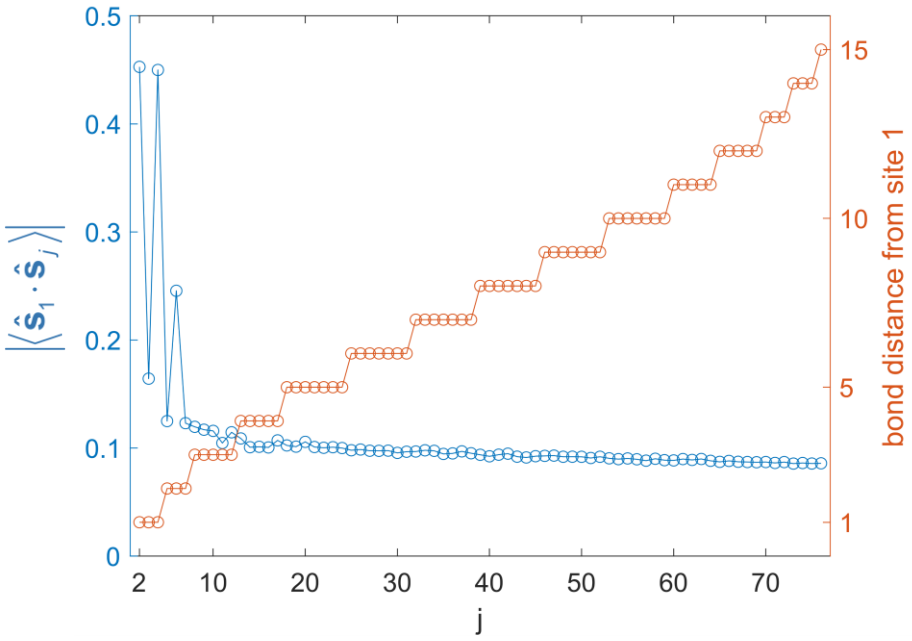

Figure 18. Magnitude of SPCFs (left y-axis; correlations are positive/negative for pairs in same/different lattices) and bond distances from reference site 1 (right y-axis) in the truncated icosidodecahedron. The site numbering follows Figure 17.

4. Conclusions

By partitioning spin sites into clusters, the cPHF method extends the variational flexibility of PHF for a simple approximation of ground states of finite Heisenberg systems. The optimization of a cluster-product state for the restoration of good quantum numbers (spin and point group) comes at a mean-field cost, with a prefactor depending on the projection-grid size. The compact representation of the cPHF wave function in terms of a projector acting on a cluster mean-field state is suitable for the calculation of various properties.

We considered only energies and spin-pair correlations, but other quantities needed for modeling EPR or INS spectra, such as spin densities or expectation values of higher-

rank local spin operators, as well as transition-density matrices, could also be obtained straightforwardly, opening a perspective for the application of cPHF to moderately large magnetic molecules. For antiferromagnetic $s = \frac{1}{2}$ spin rings, which are more challenging for PHF than $s > \frac{1}{2}$ systems [6], cPHF significantly improves over ordinary PHF by predicting rather accurate ground states for larger ring sizes. Although the cluster ansatz cannot access the full cyclic symmetry, the accuracy of cPHF improves with cluster size, where a smaller number of bonds is left to be correlated through symmetry projection.

We additionally studied hexagonal lattice fragments ($s = \frac{1}{2}$) and symmetric polyhedra ($\frac{1}{2} \leq s \leq 2$) where cluster groupings can maintain the full spatial symmetry. In these systems, it is generally advantageous to include strongly antiferromagnetic bonds in the clusters. This may be accomplished by maximizing the number of intact rings (Clar sextets) in hexagonal lattices or by defining, if possible, clusters in terms of classically unfrustrated bonds in polyhedra. Applications to the $s = 2$ truncated icosahedron and the $s = \frac{1}{2}$ truncated icosidodecahedron demonstrate that cPHF can be applied to systems whose size is prohibitive for exact diagonalization and challenging for other methods.

More advanced symmetry-projected methods have been under active development in various fields of many-body physics and appear worth pursuing for Heisenberg systems. Specifically, a linear combination of cluster-product states (configurations) is systematically improvable by increasing the number of configurations and would thus ameliorate problems associated with the lack of size-extensivity. Such a multiconfiguration variant of cPHF would also give access to excited states in the respective symmetry sectors that are needed for modeling spectra and low-temperature properties of molecular magnets.

Author Contributions: Conceptualization, S.G.T.; Methodology, S.G.T.; Formal analysis, S.G.T. and C.A.J.-H.; Writing—original draft, S.G.T.; Writing—review & editing, S.G.T. and C.A.J.-H.; Supervision, C.A.J.-H. All authors have read and agreed to the published version of the manuscript.

Funding: This research received no external funding.

Acknowledgments: S.G.T. thanks the German Academic Exchange Service (DAAD) for support in the early stages of this project.

Conflicts of Interest: The authors declare no conflict of interest.

Appendix A. Optimization of the Broken-Symmetry Reference

The self-consistent field (SCF) optimization of the cluster-product state $|\Phi\rangle$, Equation (A1),

$$|\Phi\rangle = |\Phi_1\rangle|\Phi_2\rangle \ldots |\Phi_Q\rangle = \prod_{i=1}^{Q} |\Phi_i\rangle \tag{A1}$$

in cPHF is closely analogous to the diagonalization-based PHF algorithm described in the Supplemental Material to [6]. Here, we explain gradient-based optimization [21] as an alternative approach that displays better convergence behavior for the present problem. In the following, we assume for simplicity that (i) all sites have the same local spin-quantum number s, (ii) all clusters (total number Q) contain the same number of sites q, and (iii) all nonzero interactions between pairs of spin centers (belonging to the same cluster or to different clusters) have the same strength in the Heisenberg model, $J_{ij} = 1$. We use indices i and i' for clusters ($i, i' = 1, 2, ..., Q$) and p and p' for sites in a cluster ($p, p' = 1, 2, ..., q$).

In Equation (A2), a Thouless rotation $e^{\hat{Z}}$ relates $|\Phi\rangle$ to an initial guess $\left|\Phi^0\right\rangle$:

$$|\Phi\rangle = A e^{\hat{Z}} \left|\Phi^0\right\rangle . \tag{A2}$$

A is a normalization constant. This rotation separates into rotations for all individual clusters,

$$|\Phi\rangle = \prod_{i=1}^{Q} \left(A_i e^{\hat{Z}_i} \left| \Phi_i^0 \right\rangle \right) , \tag{A3}$$

where

$$\hat{Z}_i = \sum_{v \in \text{virt}} \sum_{o \in \text{occ}} Z_{i,vo} \hat{c}_{i,v}^\dagger \hat{c}_{i,o} . \tag{A4}$$

The quantum-chemical terminology used in Equation (A4), occ = "occupied", virt = "virtual", refers to a fermionic formulation (cf. [6]), where $\left|\Phi_i^0\right\rangle$ defines a single occupied molecular orbital ($o = 1$) at the respective cluster in terms of a fermionic creation operator,

$$|\Phi_i\rangle \leftrightarrow \hat{c}_{i,o}^\dagger |0_i\rangle, \tag{A5}$$

where $|0_i\rangle$ is the vacuum at cluster i. The remaining (orthogonal) $M-1$ states, where $M = (2s+1)^q$ is the dimension of the local Hilbert space, defines a set of virtual orbitals. The $M-1$ optimization parameters $Z_{i,vo}$ are the elements of a complex column vector $\mathbf{Z}_i$ (the Thouless vector). The essence of cPHF consists of minimizing the energy E of the projected state $|\Psi\rangle = \hat{P}|\Phi\rangle$.

As indicated, we find it helpful to draw a conceptual connection to electronic-structure theory by associating the state of a spin cluster with a molecular orbital occupied by a single fermion. This is analogous to our approach to PHF [6], which can be regarded as a special case of cPHF with cluster size $q = 1$. A fermionic formulation leads to a second-quantized Hamiltonian,

$$\hat{H} = \sum_{lm} t_{lm} \hat{c}_l^\dagger \hat{c}_m + \frac{1}{2} \sum_{klmn} \hat{c}_k^\dagger \hat{c}_l^\dagger \hat{c}_m \hat{c}_n [kn|lm] , \tag{A6}$$

parameterized by one- and two-body integrals t_{lm} and $[kn|lm]$, respectively. Projection into the subspace of states that have exactly one fermion per site is implicitly assumed, such that the fermionic Hamiltonian (Equation (A6)) becomes equivalent to the Heisenberg model, $\hat{H} = \sum_{i<j} J_{ij} \hat{\mathbf{s}}_i \cdot \hat{\mathbf{s}}_j$.

Integrals in Equation (A6) have a simple block structure. The matrix $\mathbf{t}$ comprising matrix elements t_{lm} is of dimension $(Q \cdot M) \times (Q \cdot M)$ but consists of Q blocks $\mathbf{h}_i$, where $\mathbf{h}_i$ is the Hamiltonian of the i-th isolated cluster. We similarly define reduced two-body integrals $[kn|lm]_{pp'}$ (for $p, p' = 1, 2, ..., q$) for the interaction of site p of an arbitrary cluster with site p' of another arbitrary cluster. These integrals are generally zero for most combinations p, p' because only specific site pairs interact. Local spin matrices $\mathbf{s}_{p,\alpha}$ ($p = 1, 2, ..., q$; $\alpha = x, y, z$) are of dimension $M \times M$. The number Z of nonzero entries in $\mathbf{s}_{p,\alpha}$ is independent of p (for $s = \frac{1}{2}$, $Z = M$ for all α). For a given α, there are thus Z^2 combinations of nonzero entries in $\mathbf{s}_{p,\alpha}$ and $\mathbf{s}_{p',\alpha}$, each combination yielding a nonvanishing integral $[kn|lm]_{pp'}$. The value of $[kn|lm]_{pp'}$ is the product of the respective nonzero entries in $\mathbf{s}_{p,\alpha}$ and $\mathbf{s}_{p',\alpha}$ (all couplings are assumed to have the same strength, $J = 1$); (k, n) and (l, m) are the (row, column) indices of the nonzero entries in $\mathbf{s}_{p,\alpha}$ and $\mathbf{s}_{p',\alpha}$, respectively.

The initial guess $\left|\Phi_i^0\right\rangle$, that is, an initial set of molecular orbitals (MOs), is provided in terms of expansion coefficients $\mathbf{O}_{i,\text{occ}}^0$ in the uncoupled $\left|m_1, m_2, ..., m_q\right\rangle$ basis, where the latter corresponds to an orthonormal atomic-orbital (AO) basis in electronic-structure calculations. $\mathbf{O}_{i,\text{occ}}^0$ is an $M \times 1$ vector, and $\mathbf{O}_i^0 = (\mathbf{O}_{i,\text{occ}}^0, \mathbf{O}_{i,\text{virt}}^0)$ is $M \times M$. We generate $\left|\Phi_i^0\right\rangle$ through small random mixing of occupied and virtual cHF orbitals. At each iteration of the optimization process, a pure-state density matrix $\boldsymbol{\rho}_i$ for each cluster can be formed:

$$\boldsymbol{\rho}_i = \mathbf{O}_{i,\text{occ}} \mathbf{O}_{i,\text{occ}}^\dagger . \tag{A7}$$

In the first iteration, we set $\mathbf{Z} = \mathbf{0}$ and $\mathbf{O}_i = \mathbf{O}_i^0$ and calculate (as described below) the energy E of the projected state as well as the global gradient with respect $\mathbf{Z}$.

Equations (A8) and (A9) describe the updating of $\mathbf{O}_i$ through a Thouless rotation $\mathbf{Z}_i$ from $\mathbf{O}_i^0$ in each iteration. The number L_i and the lower triangular $(M-1)\times(M-1)$ matrix $\mathbf{M}_i$ are obtained from Equations (A8) and (A9) by Cholesky decomposition:

$$1+\mathbf{Z}_i^T\mathbf{Z}_i^* = L_iL_i^*, \tag{A8}$$

$$\mathbf{1}+\mathbf{Z}_i^*\mathbf{Z}_i^T = \mathbf{M}_i\mathbf{M}_i^\dagger. \tag{A9}$$

Following Equations (3.45) and (3.47) in [21], we form the intermediate $\breve{\mathbf{O}}$:

$$(\breve{\mathbf{O}}_{i,\mathrm{occ}})_k = (\mathbf{O}^0_{i,\mathrm{occ}})_k + \sum_{v=1}^{M-1}(\mathbf{Z}_i)_v(\mathbf{O}^0_{i,\mathrm{virt}})_{kv}\,, \tag{A10}$$

$$(\breve{\mathbf{O}}_{i,\mathrm{virt}})_{lm} = (\mathbf{O}^0_{i,\mathrm{virt}})_{lm} - (\mathbf{Z}_i)^*_m(\mathbf{O}^0_{i,\mathrm{occ}})_l\,, \tag{A11}$$

and finally obtain the properly orthonormalized (unitary) $\mathbf{O}_i$:

$$\mathbf{O}_{i,\mathrm{occ}} = \frac{1}{L^*}\breve{\mathbf{O}}_{i,\mathrm{occ}}\,, \tag{A12}$$

$$(\mathbf{O}_{i,\mathrm{virt}})_{lm} = \sum_{k=1}^{M-1}(\mathbf{M}_i^{-1})_{lk}(\breve{\mathbf{O}}_{i,\mathrm{virt}})_{km}\,. \tag{A13}$$

In the following, we explain the calculation of the energy E of the projected state (similar to the PHF algorithm described in [6]; see also [20]) and the calculation of the global gradient vector $\mathbf{G}$ with elements G_{vo} $(o=1)$, defined in Equation (A14):

$$\begin{gathered}\delta E = -\sum_{vo}(G_{vo}\delta Z^*_{vo} + \mathrm{c.c.}) = \\ -2\sum_{vo}(\mathrm{Re}(G_{vo})\mathrm{Re}(\delta Z_{vo}) + \mathrm{Im}(G_{vo})\mathrm{Im}(\delta Z_{vo}))\end{gathered} \tag{A14}$$

As noted above, $\mathbf{O}_i$ mediates a transformation from the AO to the MO basis. Matrices defined in the MO basis carry a tilde, where $\widetilde{\boldsymbol{\rho}}_i$ assumes a simple form:

$$\widetilde{\boldsymbol{\rho}}_i = \mathbf{O}_i^\dagger\boldsymbol{\rho}_i\mathbf{O}_i = \begin{pmatrix}\mathbf{1} & \mathbf{0}\\ \mathbf{0} & \mathbf{0}\end{pmatrix}. \tag{A15}$$

In Equation (A15), the unit matrix $\mathbf{1}$ is 1×1 because there is only one occupied MO per site. For spin projection, the grid weights $t(\Omega)$ (an Euler-angle triplet $\Omega=(\alpha,\beta,\gamma)$ defines a grid point) are combined with Wigner D-matrix elements for all combinations of magnetic quantum numbers m and k [20]:

$$x_{mk}(\Omega) = t(\Omega)D^{S*}_{mk}(\Omega)\,. \tag{A16}$$

For combined S- and PG-projection, Λ denotes a combination $\hat{R}_\Lambda = \hat{R}_\Omega\hat{R}_g$ of a spin-rotation $\hat{R}_\Omega$ and a site permutation $\hat{R}_g$. The loop over grid points $\Lambda=(\Omega,g)$ thus comprises two nested loops, for Ω and g. In the spin-rotation matrix $\mathbf{R}_\Omega$ (the matrix representation of $\hat{R}_\Omega$),

$$\mathbf{R}_\Omega = \exp(-i\alpha\boldsymbol{\tau}_z)\times\exp(-i\beta\boldsymbol{\tau}_y)\times\exp(-i\gamma\boldsymbol{\tau}_z)\,, \tag{A17}$$

$\boldsymbol{\tau}=(\boldsymbol{\tau}_x,\boldsymbol{\tau}_y,\boldsymbol{\tau}_z)$ is the total-spin vector of an isolated cluster, $\boldsymbol{\tau}_\alpha = \sum_{p=1}^{q}\mathbf{s}_{p,\alpha}$.

The PG-operation $\hat{R}_g$ converts cluster i into cluster $g(i)$, which may be associated with a permutation among sites within the clusters (internal spin permutations). Take a dimerized $(q=2)$ symmetric $N=6$ spin ring as an example (Figure A1). The cyclic operation $\hat{C}_3$ carries center $p=1$ of cluster $i=1$ into $p'=1$ of $g(i)=2$, etc., and thus does not cause internal permutations; see Figure A1a. In contrast, the vertical two-fold rotation

$\hat{C}_2$ illustrated in Figure A1b exchanges site pairs in all three clusters. In other words, the $\hat{C}_2$ operation is associated with internal permutations.

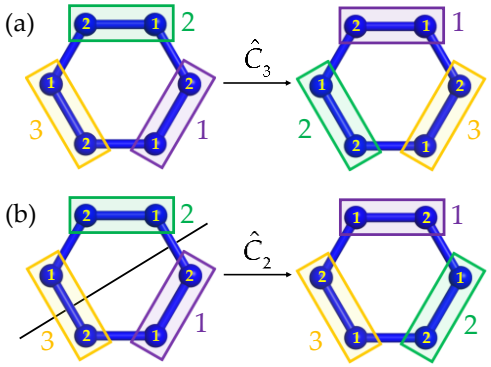

Figure A1. The cyclic point-group operation $\hat{C}_3$ keeps the numbering of spins in the clusters intact (**a**), but a vertical rotation causes internal permutations (**b**).

With $\hat{R}_g$ causing an internal spin permutation $\overline{g}(i)$ in cluster $g(i)$, the single-cluster block $\widetilde{\mathbf{R}}_{i,\Lambda}$ of the combined spin-rotation/PG-operation becomes:

$$\widetilde{\mathbf{R}}_{i,\Lambda} = \mathbf{O}_i^{\dagger}\mathbf{R}_{\Omega}\mathbf{P}_{\overline{g}(i)}\mathbf{O}_{g(i)} \,. \tag{A18}$$

$\mathbf{P}_{\overline{g}(i)}$ is the internal permutation operator. As an example, for $q = 2$, $\overline{g}(i)$ can have only two values (exchange or no exchange). For $s = \frac{1}{2}$, the exchange operator has the simple representation $\mathbf{P} = \frac{1}{2}(\mathbf{1} + 4\mathbf{s}_1 \cdot \mathbf{s}_2)$ [53]. Permutation operators for $s > \frac{1}{2}$ were derived in [54].

$\widetilde{\mathbf{R}}_{i,\Lambda}$ has four blocks,

$$\widetilde{\mathbf{R}}_{i,\Lambda} = \begin{pmatrix} \widetilde{\mathbf{R}}_{i,\Lambda}^{\mathrm{oo}} & \widetilde{\mathbf{R}}_{i,\Lambda}^{\mathrm{ov}} \\ \widetilde{\mathbf{R}}_{i,\Lambda}^{\mathrm{vo}} & \widetilde{\mathbf{R}}_{i,\Lambda}^{\mathrm{vv}} \end{pmatrix} , \tag{A19}$$

which are superscripted by o ("occupied") or v ("virtual"). Only the first column of $\widetilde{\mathbf{R}}_{i,\Lambda}$, consisting of $\widetilde{\mathbf{R}}_{i,\Lambda}^{\mathrm{oo}}$ (1×1) and $\widetilde{\mathbf{R}}_{i,\Lambda}^{\mathrm{vo}}$ $[(M-1) \times 1]$, is needed to form (i) the rotated overlap, $Q_\Lambda \equiv \langle\Phi|\hat{R}_\Omega \hat{R}_g|\Phi\rangle$, from a product of the rotated overlaps of all clusters, Equation (A20):

$$Q_\Lambda = \prod_i \widetilde{\mathbf{R}}_{i,\Lambda}^{\mathrm{oo}} \,, \tag{A20}$$

and (ii) the rotated transition-density matrices $\widetilde{\boldsymbol{\rho}}_{i,\Lambda}$:

$$\widetilde{\boldsymbol{\rho}}_{i,\Lambda} = \begin{pmatrix} \mathbf{1} & \mathbf{0} \\ \widetilde{\mathbf{R}}_{i,\Lambda}^{\mathrm{vo}} \left[\widetilde{\mathbf{R}}_{i,\Lambda}^{\mathrm{oo}}\right]^{-1} & \mathbf{0} \end{pmatrix} . \tag{A21}$$

The latter are transformed back to the AO basis:

$$\boldsymbol{\rho}_{i,\Lambda} = \mathbf{O}_i \widetilde{\boldsymbol{\rho}}_{i,\Lambda} \mathbf{O}_i^{\dagger} \,, \tag{A22}$$

and contracted with four-index interaction integrals (defined in the AO basis), Equation (A23):

$$(\Delta\mathbf{G}_{i,\Lambda})_{kl} = \sum_{mn} [kl|mn]_{pp'} (\boldsymbol{\rho}_{i',\Lambda})_{mn} \,. \tag{A23}$$

The perturbation tensor $\mathbf{G}_{i,\Lambda}$ is the sum of all $\Delta\mathbf{G}_{i,\Lambda}$ increments, as summarized in Scheme A1:

for $i = 1 : Q$ (sum over clusters)
  for $p = 1 : q$ (sum over sites in cluster i)
    for all (i', p') interacting with (i, p) (external bonds, i.e., $i \neq i'$)
      $(\Delta \mathbf{G}_{i,\Lambda})_{kl} = \sum_{mn} \left[kl \middle| mn \right]_{pp'} (\boldsymbol{\varrho}_{i',\Lambda})_{mn}$
      $(\mathbf{G}_{i,\Lambda})_{kl} = (\mathbf{G}_{i,\Lambda})_{kl} + (\Delta \mathbf{G}_{i,\Lambda})_{kl}$

Scheme A1. Incremental calculation of the perturbation tensor.

We define $\mathbf{F}_{i,\Lambda}$ as the sum of the local cluster Hamiltonian and the perturbation tensor:

$$\mathbf{F}_{i,\Lambda} = \mathbf{h}_i + \mathbf{G}_{i,\Lambda} \,. \tag{A24}$$

The quantity V_Λ is the trace of the sum $\mathbf{h}_i + \mathbf{F}_{i,\Lambda} \boldsymbol{\rho}_{i,\Lambda}$, taken over all blocks:

$$V_\Lambda = \sum_i \mathrm{Tr}\left(\mathbf{h}_i + \mathbf{F}_{i,\Lambda} \boldsymbol{\rho}_{i,\Lambda} \right) \,. \tag{A25}$$

Back in the MO basis, $\widetilde{\mathbf{F}}_{i,\Lambda} = \mathbf{O}_i^\dagger \mathbf{F}_{i,\Lambda} \mathbf{O}_i$. At each grid point Λ, the following quantities are incremented (for Equations (A28) and (A29), see Equations (3.37) and (3.38) in [21]):

$$W_{mk} \mathrel{+}= w_{\Lambda,mk} \,, \tag{A26}$$

$$H_{mk} \mathrel{+}= \frac{1}{2} w_{\Lambda,mk} V_\Lambda \,, \tag{A27}$$

$$\widetilde{\mathbb{R}}_{i,mk} \mathrel{+}= w_{\Lambda,mk} \widetilde{\mathbf{r}}_{i,\Lambda} \,, \tag{A28}$$

$$\widetilde{\mathbb{T}}_{i,mk} \mathrel{+}= w_{\Lambda,mk} \left[\frac{1}{2} V_\Lambda \widetilde{\mathbf{r}}_{i,\Lambda} + (\mathbf{1} - \widetilde{\boldsymbol{\rho}}_{i,\Lambda}) \widetilde{\mathbf{F}}_{i,\Lambda} \widetilde{\mathbf{r}}_{i,\Lambda} \right] \,, \tag{A29}$$

where $\widetilde{\mathbf{r}}_{i,\Lambda}$ denotes the first column of $\widetilde{\boldsymbol{\rho}}_{i,\Lambda}$, and $w_{\Lambda,mk}$ is defined in Equation (A30):

$$w_{\Lambda,mk} = x_{mk}(\Omega) \chi_\Gamma^*(g) Q_\Lambda \,, \tag{A30}$$

and $\chi_\Gamma^*(g)$ is an element of the character vector (the PG-projector is $\hat{P}_\Gamma = \frac{1}{h} \sum_{g=1}^{h} \chi_\Gamma^*(g) \hat{R}_g$).

The generalized eigenvalue-problem is solved for the lowest energy E:

$$\mathbf{H}\mathbf{f} = E \mathbf{W}\mathbf{f} \,, \tag{A31}$$

under the normalization constraint $\mathbf{f}^\dagger \mathbf{W} \mathbf{f} = 1$. We assemble the local gradient $\widetilde{\mathbf{g}}_i$ from the $\widetilde{\mathbb{R}}_{i,mk}$ and $\widetilde{\mathbb{T}}_{i,mk}$ sets of vectors:

$$\widetilde{\mathbf{g}}_i = -\sum_{MK} f_m^* f_k \left(\left[\widetilde{\mathbb{T}}_{i,mk} \right]_{\mathrm{virt}} - E \left[\widetilde{\mathbb{R}}_{i,mk} \right]_{\mathrm{virt}} \right) \,, \tag{A32}$$

where the notation $\left[\widetilde{\mathbb{T}}_{i,mk} \right]_{\mathrm{virt}}$ signifies that the first element of the vector $\widetilde{\mathbb{T}}_{i,mk}$ is excluded, that is, $\widetilde{\mathbf{g}}_i$ is $(M-1) \times 1$. The global gradient $\mathbf{G}_i$ is obtained by transforming to the MO basis of the initial guess [21],

$$\mathbf{G}_i = \frac{1}{L_i^*} (\mathbf{M}_i^T)^{-1} \widetilde{\mathbf{g}}_i \,. \tag{A33}$$

The $\mathbf{G}_i$ for all Q clusters is concatenated into $\mathbf{G}$, which is $Q \cdot (M-1) \times 1$. The energy E of the projected state, the initial guess $\mathbf{O}^0$, and the global gradient $\mathbf{G}$ are passed to the fminunc function in Matlab. The separation into real and imaginary parts (Equation (A14)) is required for fminunc, which optimizes with respect to a set of real variables.

Note that for cPHF with a UHF (instead of a GHF reference) we first run a few iterations with an SCF algorithm to determine the local spin-projections on the z-axis, m_i. With the initial guess thus established, we switch to gradient-based optimization, setting those elements of the gradient to zero which would change m_i. In other words, in gradient-based optimization, all m_i numbers are frozen at their values in the initial guess $\mathbf{O}^0$.

Appendix B. Spin-Pair Correlation Functions (SPCFs)

The calculation of SPCFs is analogous to the evaluation of the energy. A double-integration over the spin-projection grid can be avoided because $\hat{\mathbf{s}}_i \cdot \hat{\mathbf{s}}_j$ is a spin scalar, which commutes with the (Hermitian and idempotent) spin-projection operator. For PG-projection, we consider only one-dimensional representations Γ. Then only the totally symmetric part $(\hat{\mathbf{s}}_i \cdot \hat{\mathbf{s}}_j)_{\Gamma_1}$, Equation (A34):

$$(\hat{\mathbf{s}}_i \cdot \hat{\mathbf{s}}_j)_{\Gamma_1} = \frac{1}{h} \sum_{g=1}^{h} \hat{R}_g^\dagger (\hat{\mathbf{s}}_i \cdot \hat{\mathbf{s}}_j) \hat{R}_g \,, \tag{A34}$$

contributes to $\langle \Phi | \hat{P}_\Gamma^\dagger (\hat{\mathbf{s}}_i \cdot \hat{\mathbf{s}}_j) \hat{P}_\Gamma | \Phi \rangle$. Overall, a single summation/integration is required to evaluate SPCFs for PGSGHF wave functions [6]:

$$\langle \Phi | \hat{P}_S^\dagger \hat{P}_\Gamma^\dagger (\hat{\mathbf{s}}_i \cdot \hat{\mathbf{s}}_j) \hat{P}_S \hat{P}_\Gamma | \Phi \rangle = \langle \Phi | (\hat{\mathbf{s}}_i \cdot \hat{\mathbf{s}}_j)_{\Gamma_1} \hat{P}_S \hat{P}_\Gamma | \Phi \rangle \,. \tag{A35}$$

The evaluation of the expectation value for each term $\hat{\mathbf{s}}_l \cdot \hat{\mathbf{s}}_m$ occurring in the symmetrized operator $(\hat{\mathbf{s}}_i \cdot \hat{\mathbf{s}}_j)_{\Gamma_1}$ depends on whether sites l and m are in the same cluster (corresponding to a single-particle term) or in different clusters (two-particle term).

Appendix C. Reference Energies for Spin Rings

Singlet and triplet energies for spin rings from SUHF, SGHF and PGSGHF are collected for reference in Tables A1–A3, respectively.

Table A1. Singlet and triplet energies and the gap ΔE_{ST} in $s = \frac{1}{2}$ rings with N sites and cluster size q. SUHF predictions are compared to exact results (from Table V.1 in [32]).

		N				
q		6	12	18	24	30
2	E_{S}	−2.6514	−4.8770	−7.1335	−9.3914	−11.6485
	E_{T}	−1.8956	−4.3114	−6.6414	−8.9434	−11.2237
	ΔE_{ST}	0.756	0.566	0.492	0.448	0.425
6	E_{S}	−2.8028	−5.3482	−7.7332	−10.2071	−12.6941
	E_{T}	−2.1180	−4.7874	−7.3492	−9.8772	−12.3954
	ΔE_{ST}	0.685	0.561	0.384	0.330	0.299
Exact	E_{S}	−2.803	−5.387	−8.023	−10.670	−13.322
Exact	ΔE_{ST}	0.685	0.356	0.241	0.183	0.147

Table A2. Singlet and triplet energies and the gap ΔE_{ST} in $s = \frac{1}{2}$ rings with N sites and cluster size q. SGHF predictions are compared to exact results (from Table V.1 in [32]).

		N				
q		6	12	18	24	30
2	E_S	−2.8028	−5.0625	−7.3603	−9.6589	−11.9416
	E_T	−2.1180	−4.5485	−6.8696	−9.1446	−11.4453
	ΔE_{ST}	0.685	0.514	0.491	0.514	0.496
6	E_S	−2.8028	−5.3768	−7.9641	−10.4728	−12.9231
	E_T	−2.1180	−5.0090	−7.6042	−10.1411	−12.6090
	ΔE_{ST}	0.685	0.368	0.360	0.332	0.314
Exact	E_S	−2.803	−5.387	−8.023	−10.670	−13.322
Exact	ΔE_{ST}	0.685	0.356	0.241	0.183	0.147

Table A3. Singlet and triplet energies and the gap ΔE_{ST} in $s = \frac{1}{2}$ rings with N sites and cluster size q. D_QSGHF predictions ($Q = N/q$) are compared to exact results (from Table V.1 in [32]).

		N				
q		6	12	18	24	30
2	E_S	−2.8028	−5.3710	−7.8905	−10.3945	−12.8677
	E_T	−2.1180	−5.0104	−7.5544	−10.0287	−12.4834
	ΔE_{ST}	0.685	0.361	0.336	0.366	0.384
6	E_S	−2.8028	−5.3874	−8.0224	−10.6501	−13.2762
	E_T	−2.1180	−5.0315	−7.7782	−10.4356	−13.0870
	ΔE_{ST}	0.685	0.356	0.244	0.215	0.189
Exact	E_S	−2.803	−5.387	−8.023	−10.670	−13.322
Exact	ΔE_{ST}	0.685	0.356	0.241	0.183	0.147

References

1. Bencini, A.; Gatteschi, D. *Electron Paramagnetic Resonance of Exchange Coupled Systems*; Springer: Berlin/Heidelberg, Germany, 1990.
2. Schnack, J. Large Magnetic Molecules and What We Learn from Them. *Contemp. Phys.* **2019**, *60*, 127. [CrossRef]
3. Ghassemi Tabrizi, S.; Arbuznikov, A.; Kaupp, M. Understanding Thermodynamic and Spectroscopic Properties of Tetragonal Mn_{12} Single-Molecule Magnets from Combined Density Functional Theory/Spin-Hamiltonian Calculations. *J. Phys. Chem. A* **2016**, *120*, 6864. [CrossRef] [PubMed]
4. White, S.R. Density Matrix Formulation for Quantum Renormalization Groups. *Phys. Rev. Lett.* **1992**, *69*, 2863. [CrossRef]
5. Jiménez-Hoyos, C.A.; Henderson, T.M.; Tsuchimochi, T.; Scuseria, G.E. Projected Hartree–Fock Theory. *J. Chem. Phys.* **2012**, *136*, 164109. [CrossRef]
6. Ghassemi Tabrizi, S.; Jiménez-Hoyos, C.A. Ground States of Heisenberg Spin Clusters from Projected Hartree–Fock Theory. *Phys. Rev. B* **2022**, *105*, 35147. [CrossRef]
7. Mayer, I. The Spin-Projected Extended Hartree–Fock Method. *Adv. Quant. Chem.* **1980**, *12*, 189.
8. Jiménez-Hoyos, C.A.; Rodríguez-Guzmán, R.; Scuseria, G.E. Multi-Component Symmetry-Projected Approach for Molecular Ground State Correlations. *J. Chem. Phys.* **2013**, *139*, 204102. [CrossRef]
9. Papastathopoulos-Katsaros, A.; Jiménez-Hoyos, C.A.; Henderson, T.M.; Scuseria, G.E. Coupled Cluster and Perturbation Theories Based on a Cluster Mean-Field Reference Applied to Strongly Correlated Spin Systems. *J. Chem. Theory Comput.* **2022**, *18*, 4293. [CrossRef]
10. Potthoff, M. Cluster Extensions of Dynamical Mean-Field Theory. In *DMFT: From Infinite Dimensions to Real Materials*; Pavarini, E., Kock, E., Lichtenstein, A., Vollhardt, D., Eds.; Forschungszentrum Jülich GmbH: Jülich, Germany, 2018.
11. Waldmann, O. Symmetry and Energy Spectrum of High-Nuclearity Spin Clusters. *Phys. Rev. B* **2000**, *61*, 6138. [CrossRef]
12. Schmid, K.W.; Dahm, T.; Margueron, J.; Müther, H. Symmetry-Projected Variational Approach to the One-Dimensional Hubbard Model. *Phys. Rev. B* **2005**, *72*, 85116. [CrossRef]
13. Tinkham, M. *Group Theory and Quantum Mechanics*; McGraw-Hill: New York, NY, USA, 1964.

14. Percus, J.K.; Rotenberg, A. Exact Eigenfunctions of Angular Momentum by Rotational Projection. *J. Math. Phys.* **1962**, *3*, 928. [CrossRef]
15. Ren, Y.-Z.; Tong, N.-H.; Xie, X.-C. Cluster Mean-Field Theory Study of $J_1 - J_2$ Heisenberg Model on a Square Lattice. *J. Phys. Condens. Matter* **2014**, *26*, 115601. [CrossRef] [PubMed]
16. Jiménez-Hoyos, C.A.; Henderson, T.M.; Scuseria, G.E. Generalized Hartree–Fock Description of Molecular Dissociation. *J. Chem. Theory Comput.* **2011**, *7*, 2667. [CrossRef] [PubMed]
17. Hendeković, J. Method of Complex Molecular Orbitals. *Int. J. Quantum Chem.* **1974**, *8*, 799. [CrossRef]
18. Jiménez-Hoyos, C.A.; Rodríguez-Guzmán, R.; Scuseria, G.E. *N*-Electron Slater Determinants from Nonunitary Canonical Transformations of Fermion Operators. *Phys. Rev. A* **2012**, *86*, 52102. [CrossRef]
19. Ghassemi Tabrizi, S.; Arbuznikov, A.; Jiménez-Hoyos, C.A.; Kaupp, M. Hyperfine-Coupling Tensors from Projected Hartree–Fock Theory. *J. Chem. Theory Comput.* **2020**, *16*, 6222. [CrossRef] [PubMed]
20. Lestrange, P.J.; Williams-Young, D.B.; Petrone, A.; Jiménez-Hoyos, C.A.; Li, X. Efficient Implementation of Variation after Projection Generalized Hartree–Fock. *J. Chem. Theory Comput.* **2018**, *14*, 588. [CrossRef] [PubMed]
21. Jiménez-Hoyos, C.A. Variational Approaches to the Molecular Electronic Structure Problem Based on Symmetry-Projected Hartree–Fock Configurations. Ph.D. Thesis, Rice University, Houston, TX, USA, 2013.
22. Jiménez-Hoyos, C.A.; Rodríguez-Guzmán, R.R.; Henderson, T.M.; Scuseria, G.E. On a Dual Representation of the Goldstone Manifold. *arXiv* **2020**, arXiv:2004.05047.
23. Schurkus, H.F.; Chen, D.; O'Rourke, M.J.; Cheng, H.-P.; Chan, G.K.-L. Exploring the Magnetic Properties of the Largest Single-Molecule Magnets. *J. Phys. Chem. Lett.* **2020**, *11*, 3789. [CrossRef]
24. Lebedev, V.I.; Laikov, D.N. A Quadrature Formula for the Sphere of the 131st Algebraic Order of Accuracy. *Dokl. Math.* **1999**, *59*, 477.
25. Rivero, P.; Jiménez-Hoyos, C.A.; Scuseria, G.E. Entanglement and Polyradical Character of Polycyclic Aromatic Hydrocarbons Predicted by Projected Hartree–Fock Theory. *J. Phys. Chem. B* **2013**, *117*, 12750. [CrossRef] [PubMed]
26. Heitmann, T.; Schnack, J. Combined Use of Translational and Spin-Rotational Invariance for Spin Systems. *Phys. Rev. B* **2019**, *99*, 134405. [CrossRef]
27. Ummethum, J.; Nehrkorn, J.; Mukherjee, S.; Ivanov, N.B.; Stuiber, S.; Strässle, T.; Tregenna-Piggott, P.L.W.; Mutka, H.; Christou, G.; Waldmann, O.; et al. Discrete Antiferromagnetic Spin-Wave Excitations in the Giant Ferric Wheel Fe_{18}. *Phys. Rev. B* **2012**, *86*, 104403. [CrossRef]
28. Szabo, A.; Ostlund, N.S. *Modern Quantum Chemistry*; Dover Publications, Courier Corporation: Chelmsford, MA, USA, 1996.
29. Coffey, D.; Trugman, S.A. Magnetic Properties of Undoped. *C60 Phys. Rev. Lett.* **1992**, *69*, 176. [CrossRef]
30. Jiménez-Hoyos, C.A.; Scuseria, G.E. Cluster-Based Mean-Field and Perturbative Description of Strongly Correlated Fermion Systems: Application to the One-and Two-Dimensional Hubbard Model. *Phys. Rev. B* **2015**, *92*, 85101. [CrossRef]
31. Schnack, J. Properties of the First Excited State of Nonbipartite Heisenberg Spin Rings. *Phys. Rev. B* **2000**, *62*, 14855. [CrossRef]
32. Ummethum, J. Calculation of Static and Dynamical Properties of Giant Magnetic Molecules Using DMRG. Ph.D. Thesis, Bielefeld University, Bielefeld, Germany, 2012.
33. Schnack, J. Effects of Frustration on Magnetic Molecules: A Survey from Olivier Kahn until Today. *Dalt. Trans.* **2010**, *39*, 4677. [CrossRef]
34. Clar, E. The Aromatic Sextet and its Significance in Relation to the Stability of Aromatic Systems. In *Polycyclic Hydrocarbons*; Springer: Berlin/Heidelberg, Germany, 1964; pp. 32–39.
35. Schmidt, H.-J.; Luban, M. Classical Ground States of Symmetric Heisenberg Spin Systems. *J. Phys. A. Math. Gen.* **2003**, *36*, 6351. [CrossRef]
36. Coffey, D.; Trugman, S.A. Correlations for the $S = 1/2$ Antiferromagnet on a Truncated Tetrahedron. *Phys. Rev. B* **1992**, *46*, 12717. [CrossRef]
37. Müller, A.; Todea, A.M.; van Slageren, J.; Dressel, M.; Bögge, H.; Schmidtmann, M.; Luban, M.; Engelhardt, L.; Rusu, M. Triangular Geometrical and Magnetic Motifs Uniquely Linked on a Spherical Capsule Surface. *Angew. Chem.* **2005**, *117*, 3925. [CrossRef]
38. Botar, B.; Kögerler, P.; Hill, C.L. $[\{(Mo)Mo_5O_{21}(H_2O)_3(SO_4)\}_{12}(VO)_{30}(H_2O)_{20}]^{36-}$: A Molecular Quantum Spin Icosidodecahedron. *Chem. Commun.* **2005**, 3138–3140. [CrossRef] [PubMed]
39. Todea, A.M.; Merca, A.; Bögge, H.; Glaser, T.; Engelhardt, L.; Prozorov, R.; Luban, M.; Müller, A. Polyoxotungstates Now Also with Pentagonal Units: Supramolecular Chemistry and Tuning of Magnetic Exchange in $\{(M)M_5\}_{12}V_{30}$ Keplerates (M = Mo, W). *Chem. Commun.* **2009**, 3351–3353. [CrossRef]
40. Todea, A.M.; Merca, A.; Boegge, H.; van Slageren, J.; Dressel, M.; Engelhardt, L.; Luban, M.; Glaser, T.; Henry, M.; Mueller, A. Extending the $\{(Mo)Mo_5\}_{12}M_{30}$ Capsule Keplerate Sequence: A $\{Cr_{30}\}$ Cluster of $S = 3/2$ Metal Centers with a $\{Na(H_2O)_{12}\}$ Encapsulate. *Angew. Chemie Int. Ed.* **2007**, *46*, 6106. [CrossRef] [PubMed]
41. Müller, A.; Sarkar, S.; Shah, S.Q.N.; Bögge, H.; Schmidtmann, M.; Sarkar, S.; Kögerler, P.; Hauptfleisch, B.; Trautwein, A.X.; Schünemann, V. Archimedean Synthesis and Magic Numbers: "Sizing" Giant Molybdenum-Oxide-Based Molecular Spheres of the Keplerate Type. *Angew. Chemie Int. Ed.* **1999**, *38*, 3238. [CrossRef]
42. Müller, A.; Luban, M.; Schröder, C.; Modler, R.; Kögerler, P.; Axenovich, M.; Schnack, J.; Canfield, P.; Bud'ko, S.; Harrison, N. Classical and Quantum Magnetism in Giant Keplerate Magnetic Molecules. *ChemPhysChem* **2001**, *2*, 517. [CrossRef]

43. Krivnov, V.Y.; Shamovsky, I.L.; Tornau, E.E.; Rosengren, A. Electronic Correlation Effects in a Fullerene Molecule Studied by the Variational Monte Carlo Method. *Phys. Rev. B* **1994**, *50*, 12144. [CrossRef]
44. Sheng, D.N.; Weng, Z.Y.; Ting, C.S.; Dong, J.M. Magnetism and Pairing in a C_{60} Molecule: A Variational Monte Carlo Study. *Phys. Rev. B* **1994**, *49*, 4279. [CrossRef]
45. Flocke, N.; Schmalz, T.G.; Klein, D.J. Variational Resonance Valence Bond Study on the Ground State of C_{60} Using the Heisenberg Model. *J. Chem. Phys.* **1998**, *109*, 873. [CrossRef]
46. Konstantinidis, N.P. Unconventional Magnetic Properties of the Icosahedral Symmetry Antiferromagnetic Heisenberg Model. *Phys. Rev. B* **2007**, *76*, 104434. [CrossRef]
47. Rausch, R.; Plorin, C.; Peschke, M. The Antiferromagnetic $S = 1/2$ Heisenberg Model on the C_{60} Fullerene Geometry. *SciPost Phys.* **2021**, *10*, 87. [CrossRef]
48. Ghassemi Tabrizi, S. Point-Group Selection Rules and Universal Momentum-Transfer Dependencies for Inelastic Neutron Scattering on Molecular Spin Clusters. *Phys. Rev. B* **2021**, *103*, 214422. [CrossRef]
49. Ghassemi Tabrizi, S. Symmetry-Induced Universal Momentum-Transfer Dependencies for Inelastic Neutron Scattering on Anisotropic Spin Clusters. *Phys. Rev. B* **2021**, *104*, 14416. [CrossRef]
50. Jiménez-Hoyos, C.A.; Rodríguez-Guzmán, R.; Scuseria, G.E. Polyradical Character and Spin Frustration in Fullerene Molecules: An Ab Initio Non-Collinear Hartree–Fock Study. *J. Phys. Chem. A* **2014**, *118*, 9925. [CrossRef] [PubMed]
51. Lee, J.; Head-Gordon, M. Distinguishing Artificial and Essential Symmetry Breaking in a Single Determinant: Approach and Application to the C_{60}, C_{36}, and C_{20} Fullerenes. *Phys. Chem. Chem. Phys.* **2019**, *21*, 4763. [CrossRef] [PubMed]
52. Altmann, S.L.; Herzig, P. *Point-Group Theory Tables*; Clarendon Press: Oxford, UK, 1994.
53. Sakurai, J.J. *Modern Quantum Mechanics*, 2nd ed.; Tuan, S.F., Ed.; Addison Wesley: Reading, MA, USA, 1993.
54. Brown, H.A. A Simple Derivation of the Spin-Exchange Operator. *Am. J. Phys.* **1972**, *40*, 1696. [CrossRef]